



# 1 **Is higher resolution always better? Open-access DEM comparison for** 2 **Slope Units delineation and regional landslide prediction**

3 Mahnoor Ahmed<sup>a</sup>, Giacomo Titti<sup>b\*</sup>, Sebastiano Trevisani<sup>c</sup>, Lisa Borgatti<sup>b</sup>, Mirko Francioni<sup>a</sup>

4 <sup>a</sup>Department of Pure and Applied Sciences, University of Urbino Carlo Bo, Urbino, 61029, Italy

5 <sup>b</sup>Department of Civil, Chemical, Environmental and Materials Engineering, ALMA MATER STUDIORUM  
6 University of Bologna, Bologna, 40126, Italy

7 <sup>c</sup>Dipartimento di Culture del Progetto, University Iuav of Venice, Venezia, 30135, Italy

8 \*Correspondence to: Giacomo Titti ([giacomo.titti@unibo.it](mailto:giacomo.titti@unibo.it))

## 9 **Abstract**

10 Digital Elevation Models (DEMs) play a key role in slope instability studies, ranging from landslide detection and  
11 recognition to landslide prediction. DEMs assist these investigations by reproducing landscape morphological  
12 features and deriving relevant predisposing factors, such as slope gradient, roughness, aspect, and curvature.  
13 Additionally, DEMs are useful for delineating map units with homogeneous morphological characteristics, such  
14 as Slope Units (SUs).

15 In many cases, the selection of a DEM depends on factors like accessibility and resolution, without considering  
16 its actual accuracy. In this study, we compared freely available global DEMs (ALOS, COP, FABDEM) and a  
17 national DEM (TINITALY) with a reference DEM (local airborne LiDAR) to identify the most suitable DEM for  
18 representing fine-scale morphology and delineating SUs in the Marche Region, Italy, for landslide susceptibility  
19 mapping. Furthermore, we proposed a novel approach for selecting the optimal SUs partition.

20 The DEM comparison was based on several criteria, including elevation, residual DEMs, roughness indices, slope  
21 variations, and the ability to delineate SUs. TINITALY, resampled at a 30x30m pixel size, was found to be the  
22 most suitable DEM for representing fine-scale terrain morphology. It was then used to generate the optimal SUs  
23 partition among 18 combinations. These combinations were evaluated using both existing and newly integrated  
24 metrics alongside mapped landslide inventories to optimize terrain delineation and produce landslide  
25 susceptibility maps.

26

## 27 **Introduction**

28 Open-access global Digital Elevation Models (DEMs) have been commonly used for a vast range of  
29 geomorphological studies, which have required modelling or analysis of terrain surface in mountain environments,  
30 where these DEMs have been characterized by a marked quality deterioration (Guth et al., 2024; Trevisani et al.,  
31 2023b). One of the many uses of DEMs has been to serve as the base input for analyzing landslides morphological  
32 features, state and style of activity and generating landslide susceptibility models (Brock et al., 2020). Among  
33 multiple methods of data-driven (Ahmed et al., 2023; Lombardo et al., 2020; Lombardo and Tanyas, 2020; Titti  
34 et al., 2021a) and physical-based models (Van den Bout et al., 2021) to predict, investigate (Brenning, 2005;  
35 Pirasteh and Li, 2017; Steger et al., 2023) and detect landslides (Qin et al., 2013), the elevation model has been



36 of essential use. DEMs are utilized to derive terrain-based characteristics (Brock et al., 2020; Mahalingam and  
37 Olsen, 2016) which have been conditioned by their resolution. In the literature, DEM resolution and its influence  
38 have been tested in several aspects such as; in landslide modelling and hazard assessment (Catani et al., 2013;  
39 Claessens et al., 2005; Fenton et al., 2013; Huang et al., 2023), in 3D physical models (Qiu et al., 2022), as well  
40 as morphological quality assessment explored at regional scales (Grohmann, 2018; Hawker et al., 2019; Trevisani  
41 et al., 2023b).

42 Comparisons among DEMs to evaluate the most suitable product are based on different criteria and the results  
43 have likely varied as per the test site. Thus, even if the same criteria have been used to rank DEMs, regional  
44 topography has influenced the preference of the elevation model in different areas (Florinsky et al., 2019; Zhang  
45 et al., 2019). Landcover has been specifically important when global DEMs (Bielski et al., 2024), such as  
46 Copernicus DEM and ALOS AW3D30, have been used for deriving a Digital Terrain Model (DTM), given that  
47 most of the times these products resembled more a Digital Surface Model (DSM: Guth & Geoffroy, 2021).

48 An ongoing initiative, the Digital Elevation Model Inter-comparison eXercise (DEMIX; Strobl et al., 2021), has  
49 aimed to align methodologies allowing for criteria-based ranking of global DEMs. In the first application (Bielski  
50 et al 2024), metrics related to slope and roughness have been considered in addition to those related to elevation  
51 differences; the approach has further developed, adopting new metrics and a wide range of geomorphometric  
52 derivatives (Guth et al., 2024). Global DEMs have been commonly used in geoscientific research due to their  
53 spatial extent and public accessibility whereas national DEMs (Gesch et al., 2018; Muralikrishnan et al., 2013;  
54 Tarquini et al., 2007) have generally been tailored to represent country-specific land surface and morphology at a  
55 higher spatial resolution and accuracy to serve geoscience applications. Shuttle Radar Topography Mission  
56 (SRTM; Jarvis et al., 2008), Advanced Land Observing Satellite (ALOS; (Takaku et al., 2014), Terra Advanced  
57 Spaceborne Thermal Emission and Reflection Radiometer Global DEM (ASTER GDEM; Abrams et al., 2010)  
58 have been among the most widely used, freely accessible and initial global DEMs popularized in geomorphic  
59 analysis (Becek, 2014; Florinsky et al., 2019; Mahalingam and Olsen, 2016; Trevisani et al., 2023b; Zhang et al.,  
60 2019). However, there are many considerations to be considered for implementing these global datasets to a  
61 localized area in the frame of landslide recognition, mapping and assessment.

62 Landslide inventories and elevation models have been essential inputs for data-driven landslide models, for which  
63 the DEM has been used to derive morphological parameters such as slope angle and slope aspect. For these  
64 derivatives to be as accurate as possible in a model, the DEM quality (Claessens et al., 2005; Mahalingam and  
65 Olsen, 2016; Saleem et al., 2019) should satisfy the representation of fine-scale morphology (Chaplot et al., 2006;  
66 Florinsky, 1998). In other words, the DEM quality has significantly affected the prediction capacity of a model.  
67 The errors contained within a DEM, even when small, propagate in derivatives of elevation (Karakas et al., 2022;  
68 Mahalingam and Olsen, 2016; Pawluszek and Borkowski, 2017; Saleem et al., 2019) which have been weighed  
69 as important factors in landslide occurrence. The various available DEMs have been generated using a range of  
70 technologies. While significant efforts have been made to improve DEMs over time, the accuracy of these models  
71 has remained a critical issue. Selecting an appropriate DEM has proven to be more important than the number of  
72 DEM-derived factors used in landslide assessment (Kamiński, 2020).



73 Another use of DEMs has been the delineation of mapping units (Schlögel et al., 2018). Mapping units have been  
74 used to subdivide the study area in homogeneous, elemental units such as: administrative units (Lombardo et al.,  
75 2019), terrain units (Van Westen et al., 1997), unique condition units (Titti et al., 2021b), grid cells (Reichenbach  
76 et al., 2018) or Slope Units (SUs; Ahmed et al., 2023). SUs were initially introduced by Carrara et al. (1991) as  
77 portions of territory, presenting homogeneous morphological characteristics for landslide identification and  
78 susceptibility mapping. The SU is, according to the scale adopted, has served as a solution that adequately  
79 represents unstable slopes.

80 To assess the suitability of DEMs for landslide susceptibility and prediction, it has been essential to conduct a  
81 quality assessment of these models which has commonly referred to the spatial resolution alone. Therefore, global  
82 DSMs and a national Italian Digital Terrain Model (DTM) has been compared with a local accurate elevation  
83 model (Airborne LiDAR) in the context of terrain representation and its delineation. The Italian DTM has been  
84 already investigated in some studies, mainly focusing on hydrogeomorphology studies (Pulighe and Fava, 2013;  
85 Zingaro et al., 2021; Annis et al., 2020; Tavares da Costa et al., 2019). Accordingly, the quality evaluation from  
86 the perspective of fine-scale morphology and geomorphometric derivatives in the context of landslide science has  
87 remained an interesting aspect to elaborate on.

88 This study has aimed to optimize inputs used for representing morphological data in landslide susceptibility  
89 assessment and to understand their interactions by: identifying the most suitable DEM for accurately representing  
90 fine-scale slope morphology; proposing a new metric for analyzing optimal SU parameters for landslide  
91 susceptibility mapping, integrating landslide inventory data with landslide area and numerosity; extending and  
92 applying the methodology to test landslide susceptibility at a regional scale in the Marche Region of Central Italy.

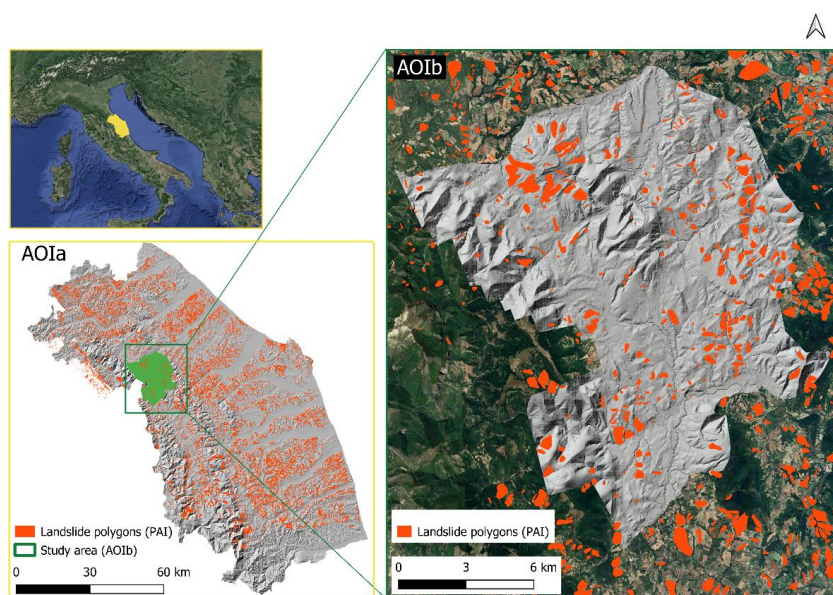
### 93 **Study Area**

94 In this study, we have selected two distinct study areas. The first Area of Interest (AOIa) has encompassed the  
95 entire Marche region, located in central-eastern Italy (Figure 1, AOIa). From the morphological point of view, this  
96 region is characterized by three different types of landforms that extend in the north-south direction. In the western  
97 part, the region has been crossed by the Apennines which can reach, in the area, a peak of 2476m a.s.l. at Monte  
98 Vettore. Then, the reliefs degrade to more rounded hills in the central part of the region till the flat eastern coastal  
99 strip. From a geological point of view, the Apennines, a Neogene fold-and-thrust belt that developed following  
100 the closure of the Mesozoic Tethys Ocean, have been characterized by calcareous units, calcareous-marly units  
101 and arenaceous, pelitic-arenaceous and marly arenaceous units (aged from Jurassic to Neogene). The hilly and  
102 coastal areas have mainly been characterized by Neocene/quadernary clayey formations. Several small rivers  
103 traverse the region from the west to the east side. In particular, the basins of Misa, Esino, Cesano, and Metauro  
104 rivers were affected by an exceptional thunderstorm in September 2022 which triggered floods and landslides  
105 (Corti et al., 2024). One of the highest rainfall intensity of the 2022 event was registered in a sub-portion of the  
106 Marche region, that has been selected as the second study area (AOIb) for this study (Figure 1, AOIb) not only  
107 because the consequences of the exceptional rainfall event but also because, morphologically, it can be considered  
108 a representative sample of the Marche mountainous region. Moreover, the area has been covered by a high-



109 resolution dataset (1m pixel size) which allows us to effectively conduct the experiments as described in the  
110 following text.

111 A relevant portion of the territory of Marche region (AOIa) presents slope failures. The most populated dataset of  
112 landslide in the area is the inventory of the Piano stralcio per l'Assetto Idrogeologico (PAI) of Marche Region  
113 (Figure 1). Click or tap here to enter text. In the area of Marche region (AOIa), the PAI inventory counts 19,296  
114 delimited landslides for a total landslide area of 1394 km<sup>2</sup> which covers 15% of the total regional surface classified  
115 as flow, slide and complex landslides.



116  
117 **Figure 1: Study area in central Italy. On the left, is the study area AOIa, encompassing the entire Marche region which**  
118 **has been analyzed in the second phase of the study. On the right is study area AOIb, a sub-portion of the Marche region**  
119 **where we conducted the DEM analysis in the first phase covered by the 1m pixel size airborne LiDAR survey. The**  
120 **Piano Stralcio per l'Assetto Idrogeologico (PAI) landslide inventory of the Marche Region identifies 19,296 landslide**  
121 **bodies as polygons (image background from © Google Maps 2019).**

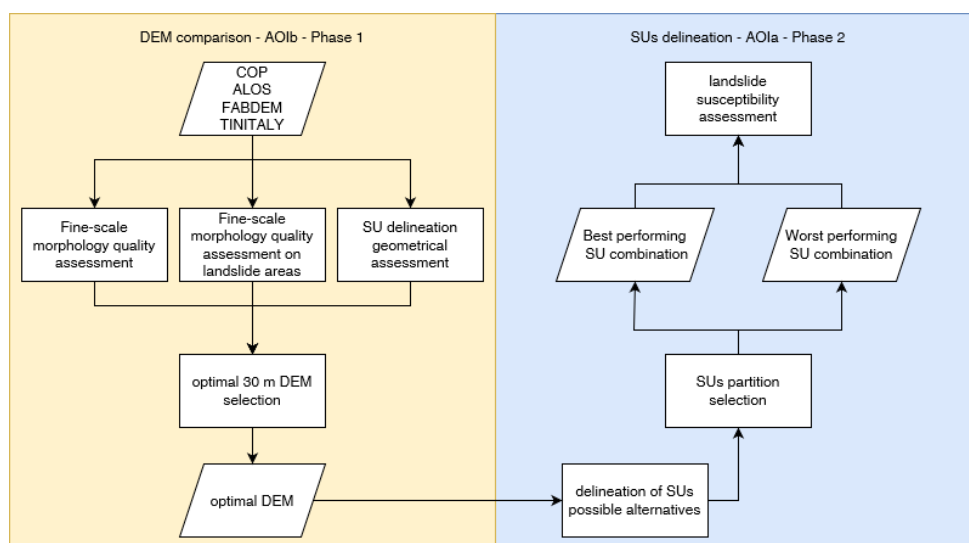
122



## 123 Materials and Methods

124 The methodology implemented in this study has aimed to assess the quality of freely available DEMs, framing  
125 their use for landslide susceptibility assessment. DEMs have been essential because they allow the derivation of  
126 landslide predisposing factors and generate a morphology-based terrain subdivision: SUs. Thus, these two uses of  
127 a DEM in landslide susceptibility assessment have been investigated.

128 The analysis has been conducted in two sequential phases (Figure 2): the first phase the differences in DEM  
129 derivatives have been assessed by comparing global and a national DEM to a local high-resolution reference  
130 elevation data in AOIb. In the second phase we have evaluated 18 SUs partitions on the base of internal/external  
131 homogeneity, landslide extension and landslide number using the best performing open-source DEM, which has  
132 been identified in the first phase of this study.



133  
134 **Figure 2: Workflow of the two-phases analysis. Phase 1 DEM assessment: comparison of global and national DEM to**  
135 **a local high-resolution reference elevation model (with reference to AOIb). Phase 2 Slope Units delineation: selection**  
136 **of the optimal parameters for SUs delineation (with reference to AOIa).**

### 137 Phase 1: DEM assessment

138 In this phase, the accuracy of three global DEM (ALOS World 3D-30m, Copernicus-GLO-30, FABDEM) and one  
139 national DEM (TINITALY) has been evaluated by a comparison with a local airborne LiDAR in the study area  
140 AOIb.

141 ALOS World 3D-30m (ALOS World 3D - 30m. V3.2, 2024) has been released by Japan Aerospace Exploration  
142 Agency (JAXA) in 2015, at a horizontal resolution of 1 arc-second, approximately 30 meters as a DSM (Caglar  
143 et al., 2018). This product, surveyed from 2006 to 2011, uses the 5-meter mesh of "World 3D Topographic Data"  
144 and is provided in two resampled versions by JAXA (mean resampling kernel is used in this study), with elevation  
145 expressed according to the Earth Gravitational Model 1996 (EGM96).



146 Copernicus-GLO-30 (COP; ESA & Sinergise, 2021), has been obtained from the WorldDEM at 1 arc second as a  
147 DSM, a product of the radar data acquisition of 12 meters TanDEM-X mission from 2011 to 2015. Forest And  
148 Buildings removed Copernicus DEM (FABDEM; Hawker et al., 2022), has been made available as a corrected  
149 global Digital Terrain Model (DTM) available at 1 arc-second grid spacing (60°S-80°N) derived from Copernicus  
150 GLO-30. Machine learning techniques have been devised to improve mean absolute vertical error in built-up and  
151 forested areas in comparison to COP (Hawker et al., 2022). Both FABDEM and COP elevations have been referred  
152 to EGM 2008 geoid.

153 TINITALY's 1.0 (Tarquini et al., 2007), and version 1.1 (Tarquini et al., 2023), has covered the whole of Italian  
154 territory, as a DTM available at 10m pixel size. Heterogenous data, mainly based on Technical Regional  
155 Cartography with elevations derived by means of photogrammetric method, has been used to build a national scale  
156 model. In particular, the Technical Regional Cartography (CTR) map scaled at 1:10000 with 10m interval for  
157 contour lines is used for Marche region in the compilation of TINITALY. A Triangular Irregular Network (TIN)  
158 structure has been employed in constructing the DEM to tackle varying data density and redundancy. Merging  
159 various types of input data is followed by significant investigation to ensure the seamless production of a high  
160 resolution and considerably the most accurate representation for Italy, with a root mean square error ranging from  
161 0.1 to 6 meters (Tarquini et al., 2007).

162 The reference DEM (as called hereafter) has been a Digital Terrain Model (DTM) acquired in 2012 using airborne  
163 LiDAR, with a pixel size of 1x1m, and a reported vertical and planimetric accuracy of 15 cm and 30 cm,  
164 respectively (Ministero dell'Ambiente e della Sicurezza Energetica, <https://gn.mase.gov.it/portale/pst-dati-lidar>).  
165 This reference DTM has been aggregated via averaging the pixel size to 30m.

166 COP, FABDEM, ALOS and TINITALY have been projected in WGS84 UTM 33N at a pixel size of 30 meters  
167 using bilinear interpolation for alignment with the reference DEM. The inclusion of COP and FABDEM, along  
168 with ALOS as a global DEM and TINITALY as a national-scale elevation model for comparison, has been invoked  
169 by several studies (Bielski et al., 2024; Guth & Geoffroy, 2021; Meadows et al., 2024; Osama et al., 2023;  
170 Trevisani et al., 2023). All the DEMs, except TINITALY (geoid model not publicly available), have been  
171 transformed to a common geoid model, EGM2008 respectively for alignment and comparison with the reference  
172 grid. TINITALY is based on the Italian geodetic network (IGM95) where the measured ground points have been  
173 described by the Italian geoid called ITALGEO 2005 (Albertella et al., 2008; Barzaghi et al., 2007). Barzaghi and  
174 Carrion (2009) have concluded that the difference between ITALGEO05 (regional geoid model) and EGM2008  
175 (global geoid model) is negligible for many applications, and both are capable to represent the region of Italy.  
176 Therefore, no geoid transformation for TINITALY has been required.

177 To perform the quality assessment of selected DEMs, elevation differences have been considered for compatibility  
178 with precedent studies. Indeed, studies focusing on DEMs comparison (Polidori and Hage, 2020) are generally  
179 based on elevation differences, using standard statistical metrics such as standard deviation and Root Mean Square  
180 Error (RMSE), and in some cases slope and aspect have been considered (Meadows et al., 2024; Zhang et al.,  
181 2019). However, as suggested in many studies (Bielski et al., 2024; Crema et al., 2020; Florinsky et al., 2019;  
182 Gesch, 2018; Guth & Geoffroy, 2021; Kakavas et al., 2020; Liu et al., 2019; Purinton & Bookhagen, 2017;  
183 Trevisani et al., 2023), statistical metrics of elevation differences alone fail to fully capture the quality of DEMs,



184 including the capability to represent fine-scale morphology and the presence of artifacts. Therefore, for this reason  
185 and because the focus of the work has been to investigate mainly the accuracy of the DEMs geomorphometric  
186 derivatives, along with the differences in elevation, a straightforward and simple approach to take the local spatial  
187 variability of surfaces into account based on a geostatistical-based methodology (Isaaks and Srivastava, 1989), as  
188 discussed by Trevisani et al. (2023b), has been proposed.

189 The approach has been based on the derivation of a residual DEM, also known as Topographic Position Index  
190 (TPI; Guisan et al., 1999; Hiller and Smith, 2008; Wilson and Gallant, 2000), and the calculation of roughness  
191 indices. The residual DEM, derived by detrending the original surface, has permitted to highlight the capability  
192 of DEMs to reproduce local fine-scale morphology. Moreover, the residual DEM has been used as input for the  
193 calculation of roughness indices such as the standard deviation of residual DEM (Grohmann et al., 2011) or even  
194 geostatistical based estimators such as the variogram (Eq 1, with  $p = 2$ ), the madogram (Eq. 1, with  $p = 1$ ) and  
195 (Eq. 2) represents the more robust Median Absolute Differences (MAD; Trevisani and Cavalli, 2016; Trevisani  
196 and Rocca, 2015). The generalization of the variogram have been described as in Eq. (1) and MAD as Eq. (2);

$$197 \gamma(\mathbf{h})_p = \frac{1}{2N(\mathbf{h})} \sum_{\alpha=1}^{N(\mathbf{h})} |z(\mathbf{u}_\alpha) - z(\mathbf{u}_\alpha + \mathbf{h})|^p = \frac{1}{2} \cdot \text{mean}(|\Delta(\mathbf{h})|^p), \quad (1)$$

198 where,

$$199 \Delta(\mathbf{h})_\alpha = z(\mathbf{u}_\alpha) - z(\mathbf{u}_\alpha + \mathbf{h})$$

$$200 \text{MAD}(\mathbf{h}) = |\Delta(\mathbf{h})_{\alpha=\text{median}}|, \quad (2)$$

201 where  $\mathbf{h}$  is the separation vector (lag) between two locations ( $u$ ),  $z(u)$  is the value of the variable of interest in  
202 the location  $u$  (e.g., residual elevation), and  $N(\mathbf{h})$  is the number of point pairs with a separation vector  $\mathbf{h}$  found in  
203 the search window considered. Accordingly, the variogram is the half of the mean squared differences  $\Delta(h)_\alpha$  and  
204 the MAD is the median of the absolute differences  $\Delta(h)_\alpha$ . It should be highlighted that there are roughness indices  
205 such as  $\text{MAD}_{k2}$  and the Radial Roughness Index (RRI) that have been calculated directly from the DEM, without  
206 detrending (Trevisani et al., 2023c, a).

207 A simple short-range omnidirectional roughness index, such as MAD calculated for lag distances of 2 pixels and  
208 circular kernel of 3 pixels, permits to analyze fine-grain roughness (see Trevisani et al., 2023a; Trevisani and  
209 Rocca, 2015 for a full discussion). The MAD omnidirectional roughness index essentially provides a measure of  
210 omnidirectional spatial variability (median differences in residual elevation) by comparing all pixel values  
211 separated by a distance of  $|\mathbf{h}|$  pixels in the considered moving window. An alternative roughness index which does  
212 not require the definition of calculation parameters is the RRI (Trevisani et al., 2023c), that has been derived to  
213 improve the popular Topographic Ruggedness Index (TRI; Riley et al., 1999).

214 All the comparisons have been done using a pixel size of 30x30m. This value was assumed because it is closer to  
215 the size of global 1 arc second DEMs, except for TINITALY which is released with a pixel size of 10x10m.  
216 TINITALY has been upscaled by mean-pixel aggregation to 30x30m pixel size. The 30m DEM (TINITALY30m)  
217 has also been compared with the 10m pixel size version (TINITALY10m) in AOIb to assess the effect of upscaling  
218 on the analysis. Given that slope, roughness indices and residual DEM are scale-dependent geomorphometric  
219 derivatives, a normalization has been done to compare the results of the differences between the derivatives at



220 different resolutions of TINITALY and the reference DEM. Accordingly, a normalized difference has been adopted  
221 for each derivative D:

$$222 \quad (D_{TINITALY} - D_{reference\ DEM}) / (D_{TINITALY} + D_{reference\ DEM}).$$

223 Finally, an additional analysis has been conducted. Since the goal of the research proposes attribution to landslide  
224 studies, the DEM-derived slope difference distribution in the landslide areas delineated by the PAI inventory is  
225 also included. To avoid overestimation of landslide areas, the overlapping polygons, primarily representing  
226 reactivations, have been merged.

227 To further assist in evaluating the quality of DEMs in the frame of landslide susceptibility assessment, the SUs  
228 have been generated using various DEMs (global and national). This has allowed for a comparison of the SUs  
229 produced from the reference EM with those derived from the global DEMs under evaluation, highlighting any  
230 differences in terrain partitioning and geometry. The software r.slopeunits (Alvioli et al., 2016) has been used to  
231 generate the SU maps, starting from the SU parameters proposed by Alvioli et al. (2016) for AOIb. After a few  
232 corrections and optimizations, the parameters have been set as: flow accumulation threshold to  $5 \times 10^5$  m<sup>2</sup>,  
233 minimum SU area as 80,000 m<sup>2</sup>, circular variance as 0.4 and clean size of 60,000 m<sup>2</sup> with the cleaning method  
234 (flag -m) that removes SU smaller than the clean size as well as removes odd-shaped polygons and SUs with  
235 width as small as two grid cells (Alvioli et al., 2016). To quantify the similarity between SUs derived from  
236 reference DEM and from each DEM under observation, the Jaccard Index (Jaccard, 1901) has been utilized to  
237 estimate Intersection-over-Union (IoU) ratio between the reference (in this case SU derived from reference DEM)  
238 and the predicted (in this case the DEM under test). The Jaccard Index can measure the segmentation of the SU  
239 in reference to the overlapping of the defined shape and similarity of terrain-representation. Ranging from 0,  
240 signifying no similarity to 1 that signifies identical sets, this index considers the combined size which is inclusive  
241 of the intersection. Hence, the higher the index value, the better delineation of terrain as per the considered  
242 reference.

#### 243 Phase 2: Slope Units delineation

244 This phase of the work has been focused on the identification of the most representative and freely available DEM  
245 to subdivide the study area in SUs for landslide modelling. Therefore, 18 SUs partitions have been generated with  
246 r.slopeunits software and then compared with landslide areas and landslide counts mapped in the AOIa to find the  
247 optimal ones. The optimal DEM obtained from the first phase has been used to test SU delineation in the study  
248 area with a range of parameters. As proposed by Alvioli et al. (2016), an aspect segmentation metric has been used  
249 to analyze the optimal parameters for the Marche region, altering two parameters: the minimum surface area of  
250 SU and the minimum circular variance for terrain, and fixing the parameters flow accumulation and clean size.

251 The aspect segmentation metric has been based on the concept of partitioning terrain by grouping pixels sharing  
252 similar aspect properties. This has been transferred to SU delineation, with the assumption, given the partitioning  
253 has been evaluated by the internal homogeneity and external heterogeneity of SU. The aspect segmentation metric  
254 can be written as:

$$255 \quad F(a, c) = \frac{v_{max} - v}{v_{max} - v_{min}} + \frac{l_{max} - l}{l_{max} - l_{min}}, \quad (3)$$





256 where  $V$  (SU homogeneity) is the local aspect variance and  $I$  is the autocorrelation which represents the external  
257 heterogeneity of the adjacent SUs and  $F$  evaluates the morphometric delineation of the SUs, explained by the  
258 minimum surface area of a SU ( $a$ ) and the minimum circular variance ( $c$ ) (see for more details, Alvioli et al.,  
259 2016). The first term of  $F$  value is estimated based on the homogeneity of pixels grouped in a single SU, thus a  
260 higher value represents a better segmentation. In the same way, on the base of the second term of Eq. 3, the greater  
261 the difference between the average aspect value of each SU and each of the relative adjacent SU, the higher is the  
262  $F$  value. Overall, from a geometrical point of view the optimal  $a$  and  $c$  combination is the one that maximizes the  
263 metric value.

264 Differently from Alvioli et al. (2016) where the Area Under the Curve (AUC) derived from landslide susceptibility  
265 assessment has been also considered in selecting the optimal SU parameters, this study proposes to compare the  
266 landslides extension ( $A$ ) and landslide density ( $D$ ) per SU. The former sums the percentage of the landslide area  
267 included inside the SU where the failure has been triggered (from the initiation point). The latter is the inverse of  
268 the average number of landslides in each SU.  $A$  and  $D$  can be expressed as;

$$269 \quad A = \frac{\sum_{i=1}^N l_i}{L_i}, \quad (4)$$

$$270 \quad \frac{1}{D} = \frac{\sum_{i=1}^N d_i}{N}, \quad (5)$$

271 where  $L_i$ , in Eq. 4, is the total landslide area of all the events triggered in the  $i^{\text{th}}$  SU,  $l_i$  is the cumulative landslides  
272 area inside the  $i^{\text{th}}$  SU which excludes the extension of landslide that occupies adjacent SUs,  $N$ , in Eq. 5, is the  
273 number of unstable SUs,  $d_i$  is the number of landslides triggered in the  $i^{\text{th}}$  SU.

$$274 \quad S(a, c) = \frac{F(a, c) - F_{\min}(a, c)}{F_{\max}(a, c) - F_{\min}(a, c)} \cdot \frac{A(a, c) - A_{\min}(a, c)}{A_{\max}(a, c) - A_{\min}(a, c)} \cdot \frac{D(a, c) - D_{\min}(a, c)}{D_{\max}(a, c) - D_{\min}(a, c)}, \quad (6)$$

275 where  $S$  is the final metric which combines  $F$ ,  $A$  and  $D$ . The optimal combination of  $a$  and  $c$  for SU delineation in  
276 the study area selected is the one that maximizes the  $S$  metric in Eq. 6. SU parameters for the experiment on entire  
277 Marche region have been tested with; flow accumulation threshold to  $10 \times 10^5$  m<sup>2</sup>, clean size of 20,000 m<sup>2</sup> with the  
278 cleaning method (flag -m). Minimum area ( $a$ ) has been tested with 40, 80, 150, 200, 300 and  $500 \times 10^3$  m<sup>2</sup> with  
279 corresponding circular variance ( $c$ ) of 0.1, 0.4 and 0.7 for each  $a$ , making 18 combinations.

280 The Susceptibility Zoning plugin (SZ-plugin), integrated with QGIS and developed by Titti et al. (2022), has been  
281 used to calculate the aspect segmentation metric ( $F$ ) and to map the landslide susceptibility in the Marche region  
282 (AOIa). This analysis has utilized the DEM selected in Phase 1 and assessed four Slope Unit (SU) delineations,  
283 ranked from highest to lowest performance, as mapping units for evaluating landslide susceptibility. The analysis  
284 has been conducted using a Generalized Additive Model (Loche et al., 2023). The covariates selection includes:  
285 lithology, from national dataset (<http://portalesgi.isprambiente.it/>), landcover (2018 CORINE,  
286 <https://land.copernicus.eu/en>) as categorical covariates. The continuous covariates have been generated using the  
287 Spatial Reduction Tool (Titti et al., 2022) from the phase 1-selected DEM as derivatives; slope angle, planar and  
288 profile curvature as ordinal covariates and northness, eastness as linear covariates. The collinearity between the  
289 predisposing factors has been evaluated by the Pearson's coefficient. The results have been validated with a 10-  
290 fold spatial cross-validation which clusters the dataset with a k-means approach (Elia et al., 2023). The overall

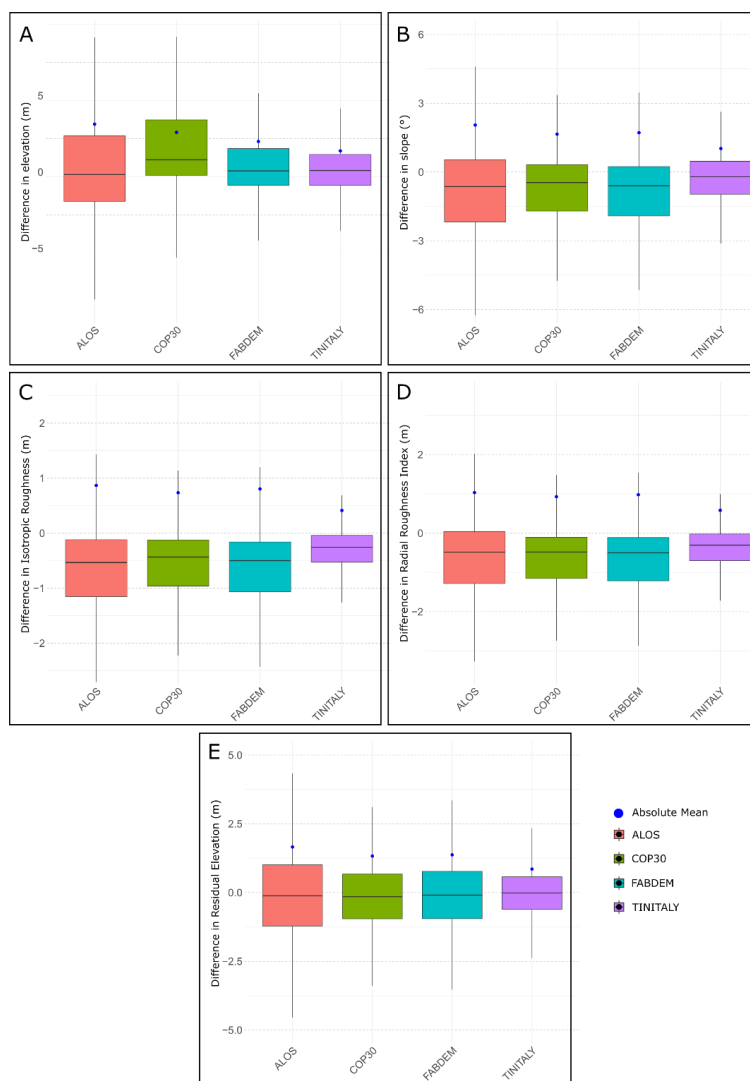


291 prediction capacity has been estimated with ROC-based AUC (Fawcett, 2006), F1 score (Singhal, 2001) and  
292 Coen's Kappa score (K; Kraemer, 2015).

### 293 **Results**

294 The differences between elevation, residual DEMs, roughness indices and slope variations within the four selected  
295 open-access DEMs and the reference DEM have been shown in Figure 3. The boxplots report the distribution of  
296 the differences highlighting the median, the first and the third quartile excluding the outliers. Moreover, since the  
297 differences report positive and negative values, the absolute mean difference has been calculated. Therefore, the  
298 lower the variance and the absolute mean difference, the better is the output considered.

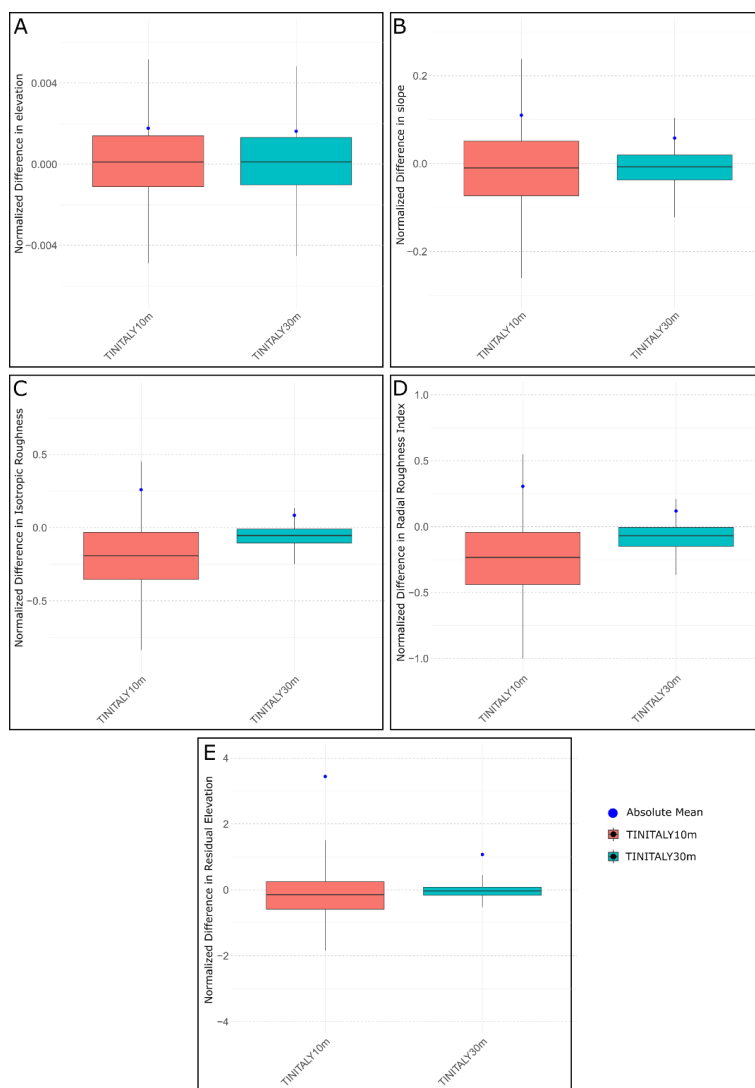
299 Overall, TINITALY resampled at 30m (TINITALY30m) has showcased the best performance across all metrics,  
300 with a smaller distribution of differences and lower absolute mean difference. ALOS, on the other hand, has  
301 displayed the largest difference among all DEMs across all metrics. Between COP and FABDEM, COP has shown  
302 a larger distribution of elevation differences, and as expected, COP has had a stronger tendency to overestimate  
303 elevation with respect to FABDEM (Figure 3). However, for slope (Figure 3B) and isotropic roughness (Figure  
304 3C), FABDEM has displayed more spread in differences.



305

306 **Figure 3:**Boxplots visualizing the differences among the DEMs at 30 meters, using different metrics with the absolute  
307 mean calculated; A) Elevation, B) Slope, C) Isotropic Roughness Index, D) Radial Roughness Index and E) Residual  
308 DEM.

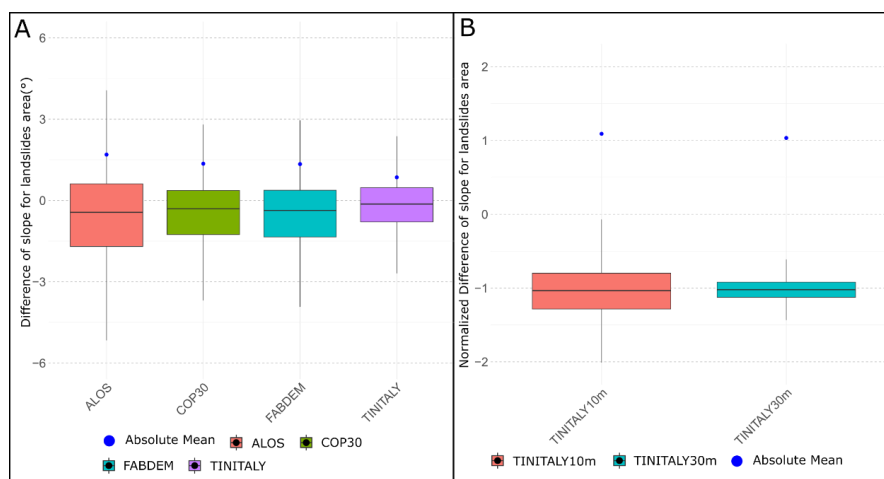
309 Figure 4 exhibits the differences of the selected derivatives between TINITALY30m and TINITALY10m. Apart  
310 the elevation, TINITALY at 10m is quantifying a larger distributions in normalized differences for the terrain  
311 indices. The absolute mean difference confirms the trend.



312

313 **Figure 4: Boxplots showing the differences in TINITALY at 10m and 30m with respect to the reference LiDAR at the**  
314 **respective resolution, for different indices with the absolute mean calculated; A) Elevation, B) Slope, C) Isotropic**  
315 **Roughness Index, D) Radial Roughness Index and E) Residual DEM.**

316 Since the main topic of our analysis is to support landslide susceptibility mapping, we have investigated the  
317 performance of the selected DEMs to derive slope, which is considered one of the most relevant landslide  
318 predisposing factors, in the area where landslide bodies have been mapped. Figure 5 shows the slope-difference  
319 within the mapped polygons of the PAI landslide inventory. TINITALY30m is seen to have the smallest differences  
320 in terms of absolute mean and the distribution among all the other DEMs (Figure 5A). Similarly, in Figure 5B,  
321 the distributions of the normalized differences of TINITALY 10m and 30m clearly highlight the larger differences  
322 distribution of the 10m DEM.



323

324 **Figure 5: A) Slope differences for 30m DEMs as compared to the reference DEM in PAI landslide polygons. B)**  
 325 **Normalized difference in slope with reference DEM for 10m and 30m TINITALY in PAI landslide polygons.**

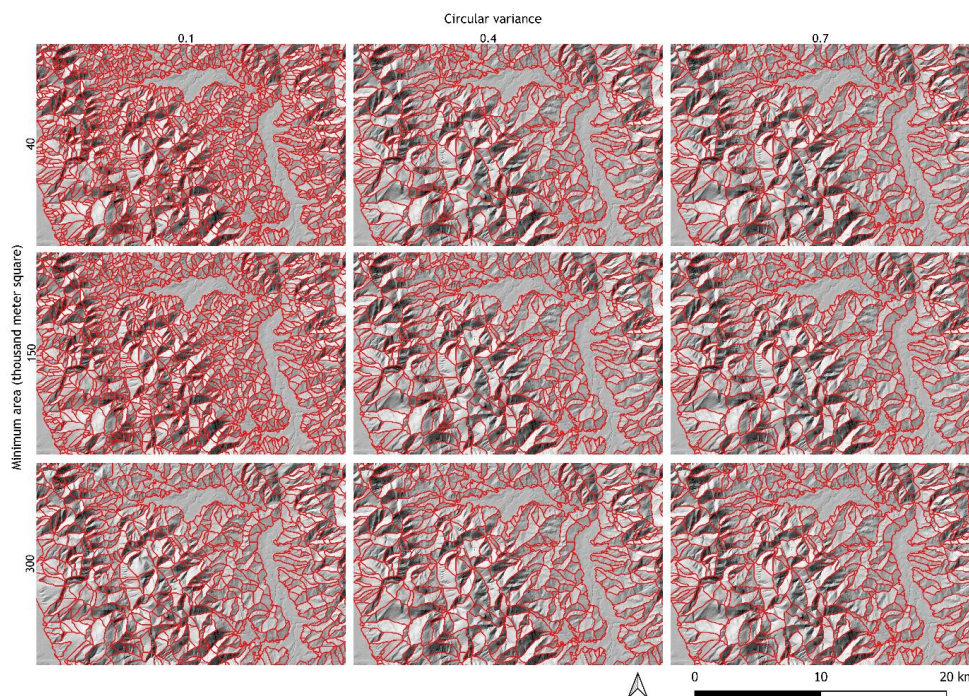
326 The last part of the DEMs comparison would investigate the effect on the SUs delineation of different DEMs.  
 327 Table 1 reports the Jaccard index tested comparing the SUs delineated with DEMs at 30m and SU generated with  
 328 the reference DEM. The highest similarity index is for TINITALY30m.

329 **Table 1: Jaccard Index represented as Intersection-over-union for SUs generated from the DEMs under test with the**  
 330 **reference LiDAR DEM SUs.**

DEM	IoU
ALOS	0.866
FABDEM	0.896
COP	0.887
TINITALY30m	0.912

331

332 The second phase of the analysis has been focused on the optimal SUs delineation to assess landslide susceptibility  
 333 in AOIa. Since in the previous analysis TINITALY30m has been found as the most accurate DEM to represent the  
 334 morphology of the mountainous area of the Marche region, we have generated 18 SU combinations based on  
 335 TINITALY30m to find the optimal SUs partition of AOIa. Figure 6 shows the visual differences in delineation for  
 336 some of the parameter combinations. Smaller values of circular variance and minimum area result in smaller  
 337 dimensions of SUs which can restrict heterogeneity between adjacent SUs while, ideally, SUs should maintain  
 338 external heterogeneity for better terrain representation.

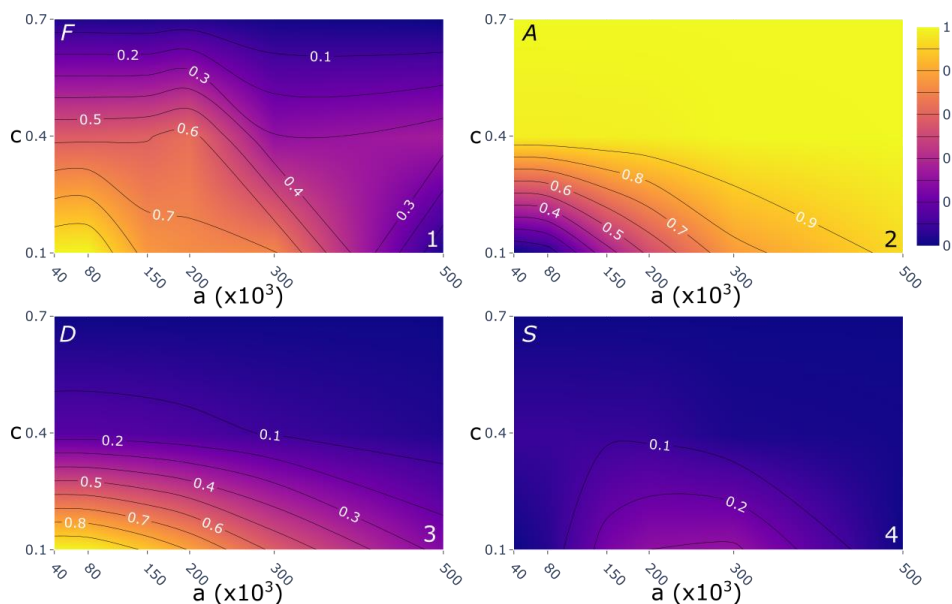


339

340 **Figure 6: SU combinations. 9 out of the 18 combinations are shown to highlight differences as the values of two**  
341 **parameters change, i.e., minimum area and circular variance.**

342 Figure 7 reports the behavior of the  $F$ ,  $A$  and  $D$  metrics and the final  $S$  metric based on the 18 combinations of  $a$   
343 and  $c$ . Considering that each of the metric represents a goodness for the final SU partition, higher the  $F$ ,  $A$  and  $D$ ,  
344 better is the SU partition. Excluding  $F$ , which shows an almost irregular pattern with the maximum at  $c$  equal to  
345 0.1 and  $a$  equal to  $40 \times 10^3 \text{ m}^2$  (Figure 7.1).  $A$  and  $D$  have a mutually opposite almost linear pattern which reach a  
346 maximum pairing: in  $A$  where  $c$  is equal to 0.7 and  $a$  is each of the values assigned (Figure 7.2), in  $D$  with  $c$  equal  
347 to 0.1 and  $a$  equal to  $40 \times 10^3 \text{ m}^2$  (Figure 7.3).  $A$  shows a better performance increasing the mapping unit extension  
348 of the study area, whereas  $D$  shows better performance with smaller partitions.

349 The product of the normalized metrics results in the  $S$  value which is maximized in the range of  $a$  between  $300 \times 10^3$   
350  $\text{m}^2$  and  $200 \times 10^3 \text{ m}^2$  and by a value of 0.1 for  $c$  (Figure 7.4). Therefore, in between the tested combination,  $c$  equal  
351 to 0.1 and  $a$  equal to  $300 \times 10^3 \text{ m}^2$  produce the optimal SU partition for landslide susceptibility mapping in the  
352 Marche region with a SU extension of  $0.40 \text{ km}^2$  on average (dataset freely available on Ahmed & Titti 2024). On  
353 the contrary the worst-case partition is the one which combines  $c$  equal to  $150 \times 10^3 \text{ m}^2$  and  $a$  equal to 0.7 with a  
354 SU extension of  $0.84 \text{ km}^2$  on average.

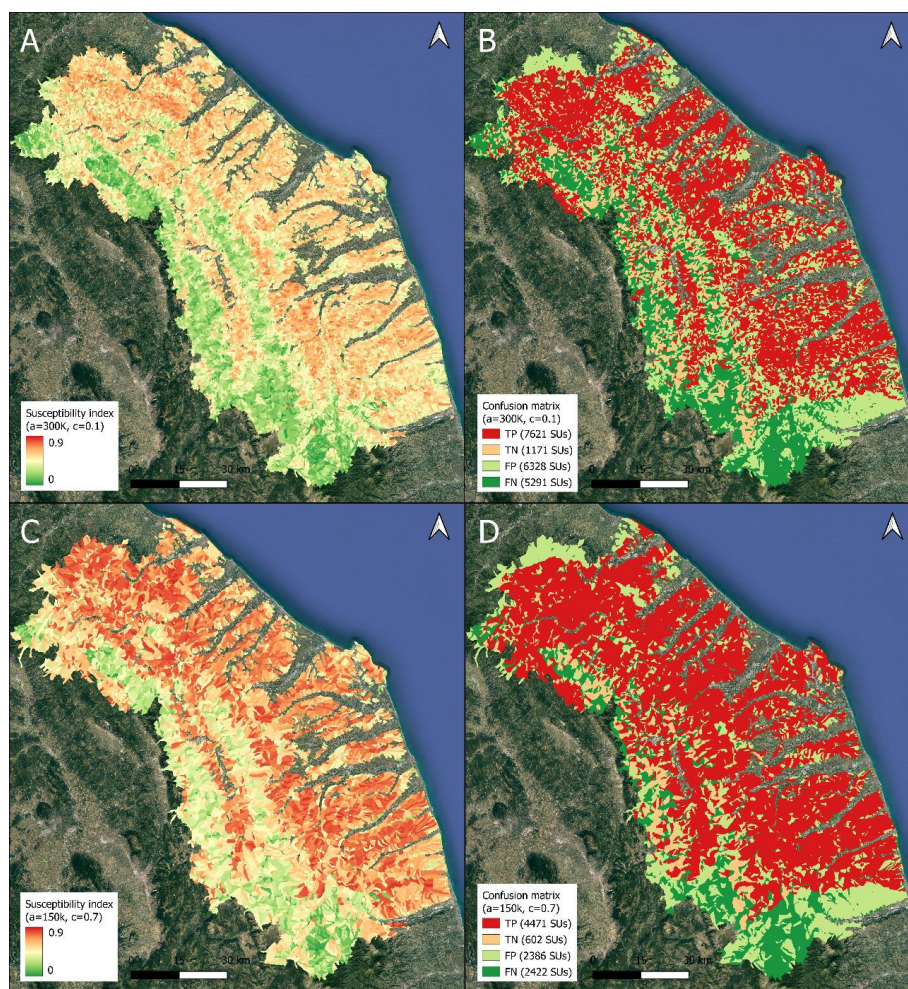


355

356 **Figure 7: Behavior of the  $F$ ,  $A$  and  $D$  metrics and the final  $S$  metric with respect to parameters  $a$  and  $c$ : (1) shows**  
357 **the  $F$  value of SU aspect segmentation metric, (2) visualizes the landslide extension inside a SU ( $A$ ), (3) shows the**  
358 **landslide density ( $D$ ) and (4) depicts the results of the final combined metric  $S$ .**

359 Consequently, the susceptibility assessment with the S-optimal and S-worst case SUs partition has been carried  
360 out. The maps resulting from the susceptibility analysis and the relative confusion matrixes based on the S-optimal  
361 and the S-worst case SUs delineation of TINITALY30m dataset are represented in Figure 8, while the quality  
362 metrics generated from the 10-fold spatial cross validation by ROC analysis are reported in Figure 9. The  
363 confusion matrix of the S-optimal delineation (Figure 8B) and of the S-worst case delineation (Figure 8D) report  
364 37% of TP (True Positive), 6% of TN (True Negative), 31% of FP (False Positive) and 26% of FN (False Negative)  
365 and 45% of TP, 6% of TN, 24% of FP and 25% of FN respectively and performance metrics equal to 0.68 of AUC,  
366 0.6 of F1 score, 0.23 of Cohen's Kappa index and 0.74 of AUC, 0.67 of F1 score, 0.29 of Cohen's Kappa index,  
367 respectively (Figure 9).

368 In addition, two more landslide susceptibility analysis have been carried out using SUs partitions with intermediate  
369 S values:  $c$  equal to  $200 \times 10^3 \text{ m}^2$  and  $a$  equal to 0.4,  $c$  equal to  $40 \times 10^3 \text{ m}^2$  and  $a$  equal to 0.1, to investigate the  
370 relation between AUC and the number, or extension, of the slope units (see Discussion section).



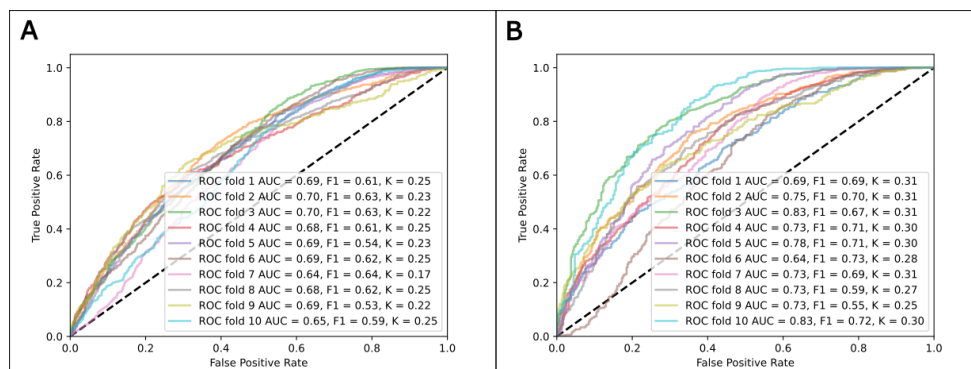
371

372 **Figure 8: Landslide susceptibility mapping with TINITALY 30m using: A) the selected optimal SU delineation**  
373 **( $a=300 \times 10^3 \text{ m}^2$ ,  $c=0.1$ ) with the relative confusion matrix (B) (TN 6% of all and 13% of unstable units); C) the selected**  
374 **worst case SU delineation ( $a=150 \times 10^3 \text{ m}^2$ ,  $c=0.7$ ) with the relative confusion matrix (D) (TN 6% of all and 12% of**  
375 **unstable units). Image background from © Google Maps 2019.**





376



377 **Figure 9: ROC curve with AUC, F1 score and Kappa coefficient values for 10-fold cross validation. A) the optimal SUs**  
378 **delineation ( $a=300 \times 10^3 \text{ m}^2$ ,  $c=0.1$ ); B) the worst-case SUs delineation ( $a=150 \times 10^3 \text{ m}^2$ ,  $c=0.7$ ).**

### 379 Discussion

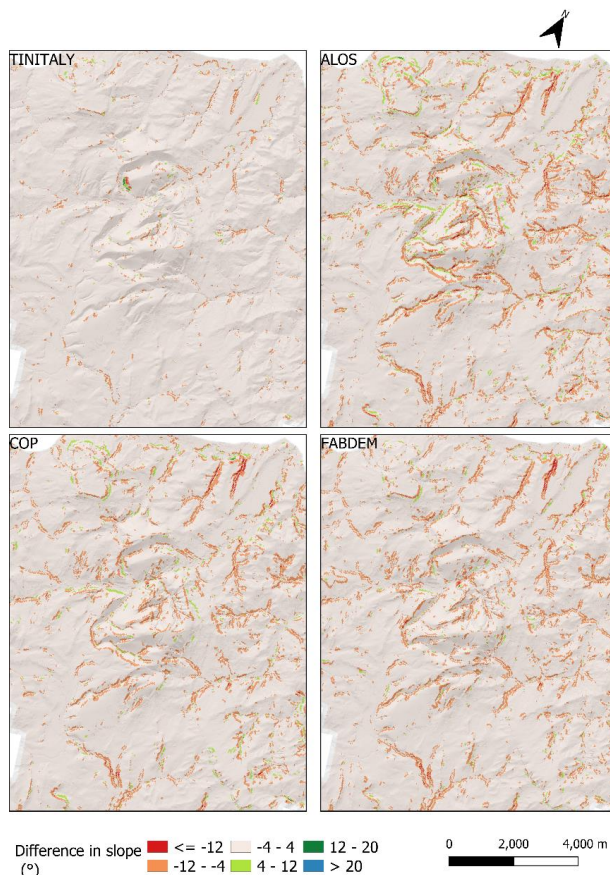
380 Based on the results of the quantitative comparison between ALOS, COP, FABDEM, TINITALY10m and  
381 TINITALY30m, the latter has performed better than the other DEMs as per the indices used in this study (Figure  
382 3). These comparisons are insightful for morphological differences for instance, in regard to roughness indices  
383 (Figure 3D), all DEMs tend to oversmooth with respect to the reference DEM. This can be indicative of the spatial  
384 support being larger than 30m in reality, meaning that the spatial data density is much lower than the given  
385 resolution. It is also interesting to realize the difference between COP and FABDEM. FABDEM being a product  
386 of COP (DSM), as a DTM, in essence it should be closer to the LiDAR representation of the terrain with vegetation  
387 and buildings removed, but it produces a less accurate output. The efforts of generating a DTM from COP have  
388 been motivated in the application of flood modelling trying to optimize the terrain representation, especially in  
389 areas of relatively low elevation. However, the algorithm has not been devised for optimizing geomorphometric  
390 derivatives such as slope (Hawker et al., 2022). This can be particularly relevant when modelling slope instability.  
391 Thus, FABDEM in the region considered does not improve the terrain representation as compared to COP (Bielski  
392 et al., 2024). This behavior is visible in Figure 3 where FABDEM shows larger difference distributions than COP  
393 for slope, residual DEM and both roughness indices. For instance, in regard to roughness indices (Figure 3D), all  
394 DEMs tend to oversmooth with respect to the reference DEM which can be indicative of the spatial support being  
395 larger than 30m in reality, meaning that the spatial data density is much lower than the given resolution.

396 ALOS consistently features high differences in all computed metrics against the counter global DEMs which  
397 could be explained with the analysis of Caglar et al. (2018). They concluded that ALOS contains a significant  
398 number of anomalies in elevation values, possibly attributed to unfiltered sensor noise and processing algorithms  
399 which are often not easily identifiable. Nonetheless, ALOS is still ranking well above other global products like  
400 SRTM and NASADEM according to quantitative assessments on DEM derived parameters and is still comparable  
401 with COP and FABDEM (Bielski et al., 2024; Guth et al., 2024).

402 The numerical comparisons resulting in Figure 3 can be supported by the graphical representation of the slope  
403 differences in Figure 10. Although the spatial distribution of differences varies, larger differences are most



404 noticeable in the ALOS DEM, followed by COP and FABDEM, compared to TINITALY30m, which exhibits  
405 fewer differences in slope compared to the reference DEM.



406

407 **Figure 10: Difference in slope (degrees) between the four tested DEMs (30m) and the reference LiDAR DEM, by**  
408 **subtracting the LiDAR value from the test DEM value.**

409 TINITALY was originally published with a pixel size of 10x10m. Since the pixel sizes of the open global DEMs  
410 selected to be compared with the reference DEM in the AOIb area are around 30x30m we have decided to conduct  
411 the entire analysis using the same grid-cell size of 30m. Therefore, the original TINITALY 10m has been resampled  
412 to 30x30m cell size. Despite this, the accuracy of TINITALY 10m has been also investigated. Therefore, we have  
413 compared the performance of TINITALY30m and of TINITALY 10m using normalized differences instead of  
414 simple differences. Although this was not the primary aim of the study, the tests indicate that TINITALY at 30m  
415 pixel size outperforms the 10m pixel size (Figure 4). These differences in performance, apart from the expected  
416 lower uncertainty related to the larger spatial support, may be attributed to the interpolation approach used for  
417 TINITALY 10m. In areas with low sampling density, noticeable artifacts appear, which can significantly affect the  
418 calculation of geomorphometric derivatives. Resampling from the original 10m pixel size to a coarser one (30m)  
419 can partially filter out these artifacts. Thus, higher resolution does not necessarily guarantee better results if it is



420 not supported by high-quality elevation data or if it contains a high number of artifacts (Chen et al., 2020;  
421 Mahalingam and Olsen, 2016). Additionally, the use of contour lines as input data along with triangulator for  
422 interpolation may result in spurious spikes at regular intervals within elevation zones and in areas with triangular  
423 slope-faces (Zingaro et al., 2021). Considering the acquisition dates of DEMs in comparison to the LiDAR,  
424 COP30 and ALOS have been surveyed closer to the time of the LiDAR than TINITALY but even so,  
425 TINITALY30m has shown better results when compared with the LiDAR. Comparing slope differences in  
426 landslide areas across the selected global open-access DEMs, as well as TINITALY10m and TINITALY30m, yield  
427 similar results. The graphs in Figure 5 present similar distribution of relative differences in Figure 3 and Figure  
428 4. Comparing slope differences in landslide areas across the selected global open-access DEMs, as well as  
429 TINITALY10m and TINITALY30m, yield similar results. The graphs in Figure 5 present similar distribution of  
430 relative differences in Figure 3 and Figure 4.

431 The similarity between the geometry of delineated SUs with the same parameters, as compared with the ones  
432 delineated from the reference DEM, indicates a higher value of the Jaccard Index for TINITALY30m. This means  
433 that the SUs delineated using TINITALY30m most closely resemble those from the reference LiDAR DEM. The  
434 remaining of the global DEMs also produce SUs with a high similarity index.

435 In the end of Phase 1, we can conclude that for the Marche region, the use 30m resampled TINITALY DEM is  
436 recommended for SU definition, therefore the rest of the analysis proposed for Phase 2 has been based on  
437 TINITALY30m.

438 Extending the analysis of SU delineation from AOIb, we have used multiple SU parameters for a more detailed  
439 analysis in AOIa with landslide polygons. A landslide can be described as a downslope movement of rock mass,  
440 earth or debris (Cruden, 1991). Understandably, slope-facing direction and slope angle can be considered as  
441 driving factors for slope failures and can be used to dissect the terrain into units which can morphologically  
442 describe landslide prone areas. Landslide susceptibility evaluates the probability of occurrence of a landslide  
443 according to a set of variables. Susceptibility depends upon a set of variables whose values are associated in a  
444 unitary manner to each mapping unit. Therefore, the mapping unit represents a portion of territory that each  
445 variable describes numerically by a single value as if it was a point object. Consequently, the smaller the dimension  
446 of the map unit, the more representative the single variable is. However, a spatial event such as a landslide, which  
447 is a non-point event, does not represent a homogeneous object according to the variables chosen to predict it (i.e.,  
448 the degree of slope is not homogeneous throughout the landslide area). Thus, to evaluate the probability of  
449 occurrence of this event, it is necessary to identify unique values for each chosen predictor calculated within a  
450 portion of territory that coincides as much as possible with the landslide. It is also comprehensible that including  
451 stable areas, the portion of territory that most closely resembles the landslide area is the slope-aspect which can  
452 be represented by the SU. Therefore, to satisfy both the needs described above, the mapping unit should be as  
453 concise as possible to describe the shape of the landslide area.

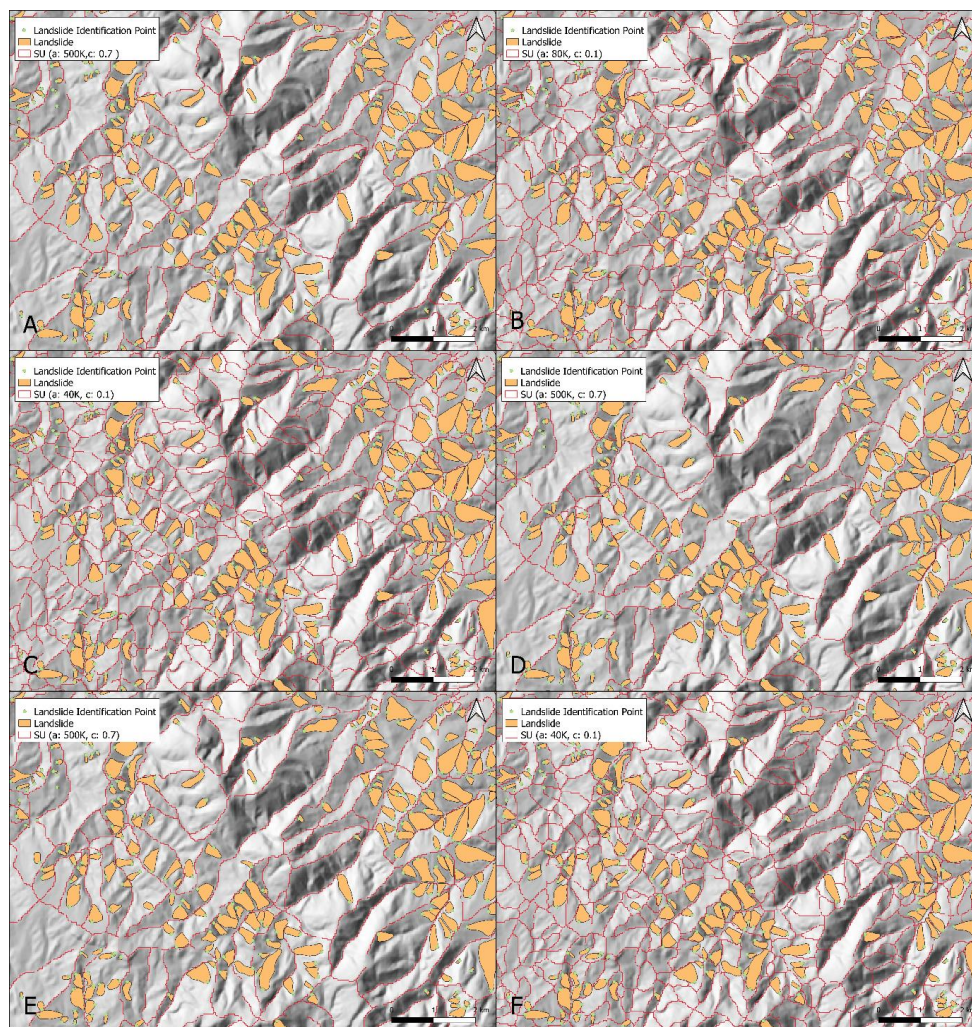
454 The methodology adopted to evaluate the SU subdivision has been designed to address the forementioned  
455 requirements by integrating new metrics, specifically tailored for landslide studies considering the relevance of  
456 terrain units with landslide inventories. In addition to the aspect segmentation metric ( $F$ ) proposed by Alvioli et  
457 al. (2016), the landslide extension coefficient ( $A$ ) and the landslide density coefficient ( $D$ ) have also been included.



458 In a way, the  $F$  metric can define the shape of the SU on the base of the spatial aspect distribution (Figure 11A  
459 and Figure 11B), while a balance between  $A$  and  $D$  can define the extension of the SU.

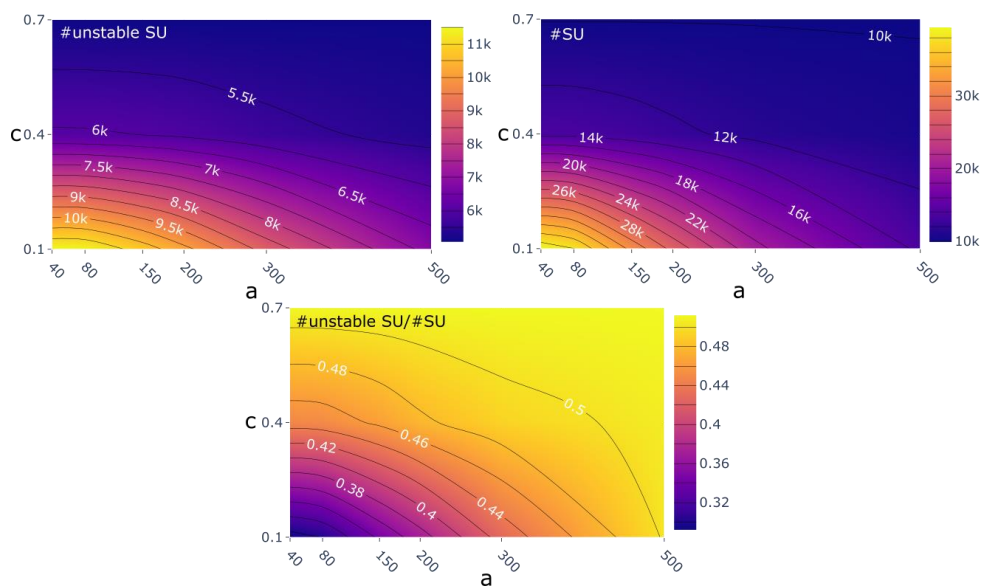
460 According to  $A$ , the optimal SUs are the ones that contain the entire landslide, with no landslide area falling in  
461 adjacent SUs. The landslide coefficient  $A$  may not fully capture the extent of landslide area especially when  
462 dealing with landslides characterized by high mobility, as in the case of flow-like landslide which can reach  
463 considerable distances where the run-out may move out from the homogenous slope-aspect. Nevertheless, the  
464 frequency distribution of the landslide classes in the landslide inventory will balance the  $A$  value, therefore the  
465 run-out of flow-like landslides may have an impact on the SU dimensions if their presence is significative in the  
466 inventory. Otherwise, part of the unstable area may fall in the adjacent SUs. Consequently, the larger the SU is,  
467 the higher is the probability of including the entire landslide, as is visible in Figure 11C and Figure 11D where an  
468 example of the lowest and highest performing SU partition according to  $A$  is represented. In contrast to  $A$ , the  $D$   
469 metric would avoid the overestimation of the SU dimension which should be limited, ideally, to a single landslide  
470 (see the example in Figure 11E and Figure 11F). A correct use of  $D$  metric requires that reactivated landslides  
471 should be excluded and considered as unique events, to avoid doubling the number of polygons in the same spatial  
472 unit.

473 The variability of the SU extension with respect to the parameters  $a$  and  $c$  can also be described through the  
474 number of unstable units in relation to the total number of SUs. Figure 12 shows how as  $D$  increases and  $A$   
475 decreases, the unstable units increase. At the same time as  $D$  increases and  $A$  decreases, the SU extension is  
476 reduced and therefore SU count increases.



477

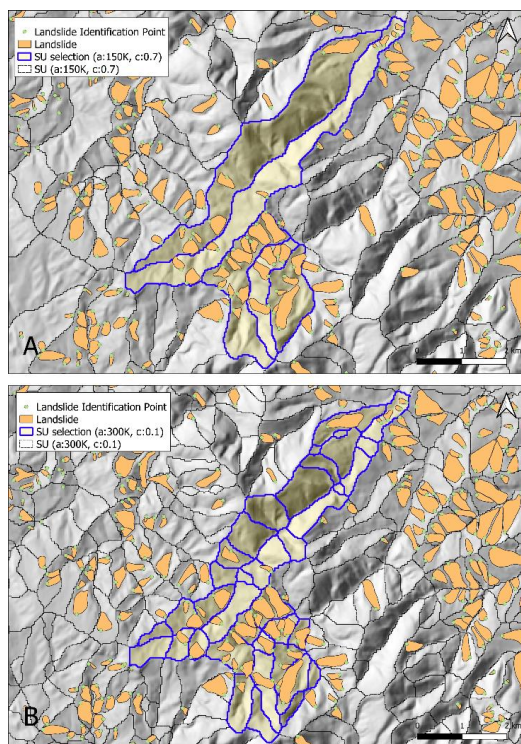
478 Figure 11: Selection of SUs partition of a sub-portion of the study area AOIa. A) and B) The SUs partitions with the  
479 lowest and the highest value of  $F$  respectively; C) and D) The SUs partitions with the lowest and the highest value of  $A$   
480 respectively; E) and F) A random selection of SUs partition with  $F$  and  $A$  values in between the highest and lowest.



481

482 **Figure 12: Evolution of the portion of unstable SUs in the study area with varying values of  $a$  and  $c$ .**

483 All metrics unified in  $S$  maximizes their effect, as shown in an example in Figure 13 where the comparable  
484 differences explain the concept of the ration between the number and extension of landslides contained in the SUs.  
485 While it is difficult to minimize SU area as well as contain the landslide area, it is to be considered that the spatial  
486 and areal accuracy of landslide inventories can significantly affect the output since the best terrain partition is  
487 interpreted based on the dimensions and number of landslide polygons. In this case study, the PAI of Marche  
488 region has been used to test the methodology, and while the landslide inventory plays a crucial role, it has to be  
489 mentioned that the dataset may come with limitations. The inventory has not been systematically updated for the  
490 mapped landslide areas and the dataset has been updated by reports from scientific literature, local authorities and  
491 projects of the municipalities (Costanzo and Irigaray, 2020). Nonetheless, the methodology remains compatible  
492 with landslide polygons and SUs supporting the selection of an optimal terrain partitioning.



493

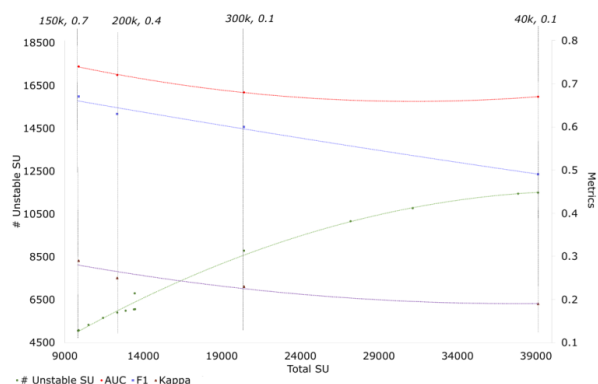
494 **Figure 13: SUs partitions of a sub-portion of the Marche study area (AOIa) compared to landslides distribution from**  
495 **the PAI. A) the SU partition ( $a: 150 \times 10^3 \text{ m}^2$  and  $c: 0.7$ ) with lowest value of  $S$ , B) the SU partition ( $a: 300 \times 10^3 \text{ m}^2$  and  $c:$**   
496  **$0.1$ ) with highest value of  $S$ .**

497 Two susceptibility analyses have been carried out selecting the  $S$ -optimal and  $S$ -worst case SUs partitions. Since,  
498 the goal of this study is not to assess landslide susceptibility of the Marche region, but to investigate the potential  
499 effect of a thought-out SUs delineation for landslide susceptibility evaluated with largely used metrics such as  
500 AUC, F1-score and Cohen's Kappa score, the predisposing factors selected for the susceptibility analysis are not  
501 entirely representative of the geo-environmental conditions. In particular, not all predisposing factors (e.g., land  
502 use, vegetation indices and others) have been considered (see also Titti et al 2024). Therefore, the cross-validation  
503 results (Figure 9A) of the susceptibility map (Figure 8A) calculated with the optimal SU subdivision are not  
504 performing high in the metrics considered (AUC = 0.68, F1 score = 0.6, K = 0.23 on average). Nevertheless, it is  
505 interesting to highlight the trend of the relation between the mapping unit extension and the AUC value along with  
506 other metrics.

507 AUC is calculated as the integral of the ROC curve. The ROC curve depends on the balance between unstable  
508 units and stable units in the training dataset, thus, the higher is the ratio between the number of unstable SUs and  
509 the total number of SUs, higher is the AUC because higher is the learning capacity of the model to recognize True  
510 Positive mapping units increasing the True Positive Rate value of the ROC curve. In the 18 combinations selected,  
511 to investigate the highest-performing  $a$  and  $c$  values for SUs delineation, we haven't changed the landslide number  
512 but the extension of the SUs whose trend is visible through the number of SUs pattern in Figure 14. Considering



513 all the combinations of  $a$  and  $c$  performed in our experiment, the higher the extension of the mapping units, the  
514 higher the proportion between the number of unstable units and the number of all the mapping units and higher  
515 the AUC (Figure 14). Same considerations can be done for the F1 score, and the Cohen's Kappa index whose  
516 behaviors follow similar trend of the AUC.



517

518 **Figure 14: Trend of the number of unstable and total SUs comparison (of 18 combinations for  $a$  and  $c$ ) and the behavior**  
519 **of the metrics resulting from the landslide susceptibility analysis. The parameters ( $a$ ,  $c$ ) are labelled along the**  
520 **performance metrics to represent the respective trend.**

521 Therefore, at least in the experiments made for this study, the metrics selected are not suitable for comparing  
522 susceptibility maps directly because the training datasets are differently balanced. Nevertheless, a comparison  
523 between the S-optimal and S-worst case susceptibility maps, as shown in Figure 8A and Figure 8C respectively,  
524 can still be made. Graphically, the maps exhibit a similar spatial pattern of landslide probability of occurrence.  
525 This is further supported by the fact that the number of True Negative units relative to unstable units is nearly the  
526 same, at 13% and 12% for the S-optimal and the S-worst case, respectively. The primary distinction lies in the  
527 susceptibility value, which is on average lower in the S-optimal delineation than in the S-worst case. This  
528 difference is attributed to the overestimation of unstable units in the S-worst case due to the imbalance between  
529 stable and unstable units.

### 530 Conclusions

531 This study encompasses DEM utilization from the viewpoint of fine-scale morphology and terrain sub-division  
532 into mapping units in the frame of regional predictive landslide modelling. The aim is to compare freely available  
533 global and national DEMs from which morphological landslide predisposing factors and optimized terrain  
534 partition in slope units are derived to map landslide susceptibility. Therefore, the investigation initially identified  
535 the optimal DEM among the available ones and then selected the optimal SUs partition in the alternative  
536 combinations generated.

537 The global DEMs (ALOS, COP, FABDEM) and TINITALY resampled at 30m have shown considerable  
538 differences with respect to the reference DEM (an airborne LiDAR resampled at 30m pixel size) in the selected  
539 geomorphometric derivatives in AOIb. Concerning the SUs delineation, the TINITALY30m has shown the best





540 performance thus, it has been selected to generate 18-parameter SUs subdivisions in AOIa. To define the optimal  
541 SUs delineation, a novel method has been proposed, which evaluates the SUs alternatives on the base of internal  
542 aspect homogeneity/external heterogeneity, landslides numerosity and landslides extension. According to the *S*  
543 metric (Eq. 6), the SUs partition generated with *c* equal to 0.1 and *a* equal to  $300 \times 10^3 \text{ m}^2$  results in the optimal  
544 subdivision, contrasting with *c* equal to 0.7 and *a* equal to  $150 \times 10^3 \text{ m}^2$  as the worst case one.

545 Ultimately, to understand the effect of the terrain partition on the landslide susceptibility model, we have  
546 performed the *S*-optimal and the *S*-worst case landslide susceptibility. It is understood that the performance  
547 metrics (AUC, F1, K) of the landslide susceptibility models do not necessarily equate with the *S* metric  
548 performance. Indeed, AUC, F1 and K depict opposite trends as compared with the *S* metric.

549 Though only TINITALY30m has been used in extending the analysis for SU experiments, COP30, as the second-  
550 best performing DEM for fine-scale morphology, can also be considered in future studies. A holistic comparison  
551 could help evaluate its effectiveness in landslide susceptibility studies. Moreover, since the result of the *S*-method  
552 depends on the landslide inventory, further research would pave the way for space-time inventories performing  
553 multi-temporal SUs delineations to reach the best terrain delineation for slope failure prediction. Developing  
554 space-time landslide inventories and adapting SUs delineation for dynamic, evolving terrains could significantly  
555 enhance the predictive capability of landslide models. Ultimately, continued innovation in DEM selection, SU  
556 partitioning methods, and landslide inventory development will contribute to more effective landslide risk  
557 management strategies and mitigation efforts.

#### 558 **Data availability**

559 The optimal SUs partition of the Marche study area (AOIa) is freely available at Ahmed and Titti (2024).

#### 560 **Author contributions**

561 MA: Conceptualization, Methodology, Formal analysis, Writing - Original Draft; GT: Conceptualization,  
562 Methodology, Formal analysis, Writing - Original Draft, Funding acquisition; ST: Methodology, Formal analysis,  
563 Writing - Review & Editing; LB: Writing - Review & Editing, Supervision; MF: Writing - Review & Editing,  
564 Supervision.

#### 565 **Competing interests**

566 The authors declare that they have no conflict of interest.

#### 567 **Acknowledgements**

568 This study was carried out within the RETURN Extended Partnership and received funding from the European  
569 Union Next480 Generation EU (National Recovery and Resilience Plan – NRRP, Mission 4, Component 2,  
570 Investment 1.3 – D.D. 1243 2/8/2022, PE0000005).



572        **References**

- 573        Abrams, M., Bailey, B., Tsu, H., and Hato, M.: The ASTER Global DEM, Photogramm Eng  
574        Remote Sensing, 76, 344–348, 2010.
- 575        Ahmed, M. and Titti, G.: Slope Units delineation for Marche region in Italy [Dataset],  
576        <https://doi.org/https://doi.org/10.5281/zenodo.13769104>, 2024.
- 577        Ahmed, M., Tanyas, H., Huser, R., Dahal, A., Titti, G., Borgatti, L., Francioni, M., and  
578        Lombardo, L.: Dynamic rainfall-induced landslide susceptibility: A step towards a unified  
579        forecasting system, International Journal of Applied Earth Observation and Geoinformation,  
580        125, 103593, <https://doi.org/10.1016/J.JAG.2023.103593>, 2023.
- 581        Albertella, A., Barzaghi, R., Carrion, D., and Maggi, A.: The joint use of gravity data and  
582        GPS/levelling undulations in geoid estimation procedures, Bollettino di Geodesia e Scienze  
583        Affini, 67, 49–59, 2008.
- 584        Alvioli, M., Marchesini, I., Reichenbach, P., Rossi, M., Ardizzone, F., Fiorucci, F., and Guzzetti,  
585        F.: Automatic delineation of geomorphological slope units with r.slopeunits v1.0 and their  
586        optimization for landslide susceptibility modeling, Geosci Model Dev, 9, 3975–3991,  
587        <https://doi.org/10.5194/gmd-9-3975-2016>, 2016.
- 588        Barzaghi, R. and Carrion, D.: Testing EGM2008 in the Central Mediterranean area, in: External  
589        Quality Evaluation Reports of EGM08, International Association of Geodesy and International  
590        Gravity Field Service, 133–143, 2009.
- 591        Barzaghi, R., Borghi, A., Carrion, D., and Sona, G.: Refining the estimate of the Italian quasi-  
592        geoid, Bollettino di Geodesia e Scienze Affini, 50, 145–159, 2007.
- 593        Becek, K.: Assessing global digital elevation models using the runway method: The advanced  
594        spaceborne thermal emission and reflection radiometer versus the shuttle radar topography  
595        mission case, IEEE Transactions on Geoscience and Remote Sensing, 52, 4823–4831,  
596        <https://doi.org/10.1109/TGRS.2013.2285187>, 2014.
- 597        Bielski, C., Lopez-Vazquez, C., Grohmann, C. H., Guth, P. L., Hawker, L., Gesch, D., Trevisani,  
598        S., Herrera-Cruz, V., Riazanoff, S., Corseaux, A., Reuter, H. I., and Strobl, P.: Novel approach  
599        for ranking DEMs: Copernicus DEM improves one arc second open global topography, IEEE  
600        Transactions on Geoscience and Remote Sensing, 62, 1–22,  
601        <https://doi.org/10.1109/TGRS.2024.3368015>, 2024.
- 602        Van den Bout, B., Lombardo, L., Chiyang, M., van Westen, C., and Jetten, V.: Physically-based  
603        catchment-scale prediction of slope failure volume and geometry, Eng Geol, 284, 105942,  
604        <https://doi.org/10.1016/J.ENGGEOL.2020.105942>, 2021.
- 605        Brenning, A.: Spatial prediction models for landslide hazards: review, comparison and  
606        evaluation, Natural Hazards and Earth System Sciences, 5, 853–862,  
607        <https://doi.org/10.5194/NHESS-5-853-2005>, 2005.
- 608        Brock, J., Schratz, P., Petschko, H., Muenchow, J., Micu, M., and Brenning, A.: The  
609        performance of landslide susceptibility models critically depends on the quality of digital  
610        elevation models, Geomatics, Natural Hazards and Risk, 11, 1075–1092,  
611        <https://doi.org/10.1080/19475705.2020.1776403>, 2020.



- 612 Caglar, B., Becek, K., Mekik, C., and Ozendi, M.: On the vertical accuracy of the ALOS world  
613 3D-30m digital elevation model, *Remote Sensing Letters*, 9, 607–615,  
614 <https://doi.org/10.1080/2150704X.2018.1453174>, 2018.
- 615 Carrara, A., Cardinali, M., Detti, R., Guzzetti, F., Pasqui, V., and Reichenbach, P.: GIS  
616 techniques and statistical models in evaluating landslide hazard, *Earth Surf Process Landf*, 16,  
617 427–445, <https://doi.org/10.1002/ESP.3290160505>, 1991.
- 618 Catani, F., Lagomarsino, D., Segoni, S., and Tofani, V.: Landslide susceptibility estimation by  
619 random forests technique: Sensitivity and scaling issues, *Natural Hazards and Earth System*  
620 *Sciences*, 13, 2815–2831, <https://doi.org/10.5194/NHESS-13-2815-2013>, 2013.
- 621 Chaplot, V., Darboux, F., Bourennane, H., Legu dois, S., Silvera, N., and Phachomphon, K.:  
622 Accuracy of interpolation techniques for the derivation of digital elevation models in relation to  
623 landform types and data density, *Geomorphology*, 77, 126–141,  
624 <https://doi.org/10.1016/J.GEOMORPH.2005.12.010>, 2006.
- 625 Chen, Z., Ye, F., Fu, W., Ke, Y., and Hong, H.: The influence of DEM spatial resolution on  
626 landslide susceptibility mapping in the Baxie River basin, NW China, *Natural Hazards*, 101,  
627 853–877, <https://doi.org/10.1007/S11069-020-03899-9/FIGURES/12>, 2020.
- 628 Claessens, L., Heuvelink, G. B. M., School, J. M., and Veldkamp, A.: DEM resolution effects  
629 on shallow landslide hazard and soil redistribution modelling, *Earth Surf Process Landf*, 30,  
630 461–477, <https://doi.org/10.1002/ESP.1155>, 2005.
- 631 Corti, M., Francioni, M., Abbate, A., Papini, M., and Longoni, L.: ANALYSIS AND  
632 MODELLING OF THE SEPTEMBER 2022 FLOODING EVENT IN THE MISA BASIN,  
633 *Italian Journal of Engineering Geology and Environment*, 69–76,  
634 <https://doi.org/10.4408/IJEGE.2024-01.S-08>, 2024.
- 635 Costanzo, D. and Irigaray, C.: Comparing Forward Conditional Analysis and Forward Logistic  
636 Regression Methods in a Landslide Susceptibility Assessment: A Case Study in Sicily,  
637 *Hydrology*, 7, 37, <https://doi.org/10.3390/HYDROLOGY7030037>, 2020.
- 638 Crema, S., Llena, M., Calsamiglia, A., Estrany, J., Marchi, L., Vericat, D., and Cavalli, M.: Can  
639 inpainting improve digital terrain analysis? Comparing techniques for void filling, surface  
640 reconstruction and geomorphometric analyses, *Earth Surf Process Landf*, 45, 736–755,  
641 <https://doi.org/10.1002/ESP.4739>, 2020.
- 642 Cruden, D. M.: A simple definition of a landslide, *Bulletin of the International Association of*  
643 *Engineering Geology - Bulletin de l'Association Internationale de G ologie de l'Ing nieur*, 43,  
644 27–29, <https://doi.org/10.1007/BF02590167>, 1991.
- 645 Elia, L., Castellaro, S., Dahal, A., and Lombardo, L.: Assessing multi-hazard susceptibility to  
646 cryospheric hazards: Lesson learnt from an Alaskan example, *Science of The Total Environment*,  
647 898, 165289, <https://doi.org/10.1016/J.SCITOTENV.2023.165289>, 2023.
- 648 Copernicus Global Digital Elevation Model:
- 649 Fawcett, T.: An introduction to ROC analysis, *Pattern Recognit Lett*, 27, 861–874,  
650 <https://doi.org/10.1016/J.PATREC.2005.10.010>, 2006.
- 651 Fenton, G. A., McLean, A., Nadim, F., and Griffiths, D. V.: Landslide hazard assessment using  
652 digital elevation models, *Canadian Geotechnical Journal*, 50, 620–631,  
653 <https://doi.org/10.1139/CGJ-2011-0342>, 2013.



- 654 Florinsky, I. V.: Accuracy of local topographic variables derived from digital elevation models,  
655 International Journal of Geographical Information Science, 12, 47–62,  
656 <https://doi.org/10.1080/136588198242003>, 1998.
- 657 Florinsky, I. V., Skrypitsyna, T. N., Trevisani, S., and Romaikin, S. V.: Statistical and visual  
658 quality assessment of nearly-global and continental digital elevation models of Trentino, Italy,  
659 Remote Sensing Letters, 10, 726–735, <https://doi.org/10.1080/2150704X.2019.1602790>, 2019.
- 660 Gesch, D. B.: Best practices for elevation-based assessments of sea-level rise and coastal  
661 flooding exposure, Front Earth Sci (Lausanne), 6,  
662 <https://doi.org/10.3389/FEART.2018.00230/BIBTEX>, 2018.
- 663 Gesch, D. B., Evans, G. A., Oimoen, M. J., and Arundel, S.: The National Elevation Dataset, in:  
664 Digital Elevation MoFDigital Elevation Model Technologies and Applications: The DEM Users  
665 Manual, American Society for Photogrammetry and Remote Sensing, 83–110, 2018.
- 666 Grohmann, C. H.: Evaluation of TanDEM-X DEMs on selected Brazilian sites: Comparison with  
667 SRTM, ASTER GDEM and ALOS AW3D30, Remote Sens Environ, 212, 121–133,  
668 <https://doi.org/10.1016/J.RSE.2018.04.043>, 2018.
- 669 Grohmann, C. H., Smith, M. J., and Riccomini, C.: Multiscale analysis of topographic surface  
670 roughness in the Midland Valley, Scotland, IEEE Transactions on Geoscience and Remote  
671 Sensing, 49, 1200–1213, <https://doi.org/10.1109/TGRS.2010.2053546>, 2011.
- 672 Guisan, A., Weiss, S. B., and Weiss, A. D.: GLM versus CCA spatial modeling of plant species  
673 distribution, Plant Ecol, 143, 107–122, <https://doi.org/10.1023/A:1009841519580/METRICS>,  
674 1999.
- 675 Guth, P. L. and Geoffroy, T. M.: LiDAR point cloud and ICESat-2 evaluation of 1 second global  
676 digital elevation models: Copernicus wins, Transactions in GIS, 25, 2245–2261,  
677 <https://doi.org/10.1111/TGIS.12825>, 2021.
- 678 Guth, P. L., Trevisani, S., Grohmann, C. H., Lindsay, J., Gesch, D., Hawker, L., and Bielski, C.:  
679 Ranking of 10 Global One-Arc-Second DEMs Reveals Limitations in Terrain Morphology  
680 Representation, Remote Sens (Basel), 16, 3273, <https://doi.org/10.3390/RS16173273>, 2024.
- 681 Hawker, L., Neal, J., and Bates, P.: Accuracy assessment of the TanDEM-X 90 Digital Elevation  
682 Model for selected floodplain sites, Remote Sens Environ, 232, 111319,  
683 <https://doi.org/10.1016/J.RSE.2019.111319>, 2019.
- 684 Hawker, L., Uhe, P., Paulo, L., Sosa, J., Savage, J., Sampson, C., and Neal, J.: A 30 m global  
685 map of elevation with forests and buildings removed, Environmental Research Letters, 17,  
686 <https://doi.org/10.1088/1748-9326/AC4D4F>, 2022.
- 687 Hiller, J. K. and Smith, M.: Residual relief separation: digital elevation model enhancement for  
688 geomorphological mapping, Earth Surf Process Landf, 33, 2266–2276,  
689 <https://doi.org/10.1002/ESP.1659>, 2008.
- 690 Huang, F., Teng, Z., Guo, Z., Catani, F., and Huang, J.: Uncertainties of landslide susceptibility  
691 prediction: Influences of different spatial resolutions, machine learning models and proportions  
692 of training and testing dataset, Rock Mechanics Bulletin, 2,  
693 <https://doi.org/10.1016/J.ROCKMB.2023.100028>, 2023.
- 694 Isaaks, E. H. and Srivastava, R. Mohan.: Applied geostatistics, Oxford University Press,  
695 London, 1989.



- 696 Jaccard, P.: Etude comparative de la distribution florale dans une portion des Alpes et du Jura,  
697 142nd ed., edited by: Bulletin de la Société vaudoise des sciences naturelles, Impr. Corbaz,  
698 1901.
- 699 ALOS World 3D - 30m. V3.2: Distributed by OpenTopography.  
700 <https://doi.org/10.5069/G94M92HB>. Accessed: 2024-04-16, last access: 18 March 2024.
- 701 Jarvis, A., Guevara, E., Reuter, H. I., and Nelson, A. D.: Hole-filled SRTM for the globe :  
702 version 4, <https://doi.org/10.2/JQUERY.MIN.JS>, 2008.
- 703 Kakavas, M., Kyriou, A., and Nikolakopoulos, K. G.: Assessment of freely available DSMs for  
704 landslide-rockfall studies, in: Proceedings of SPIE, <https://doi.org/10.1117/12.2573604>, 2020.
- 705 Kamiński, M.: The Impact of Quality of Digital Elevation Models on the Result of Landslide  
706 Susceptibility Modeling Using the Method of Weights of Evidence, *Geosciences (Basel)*, 10,  
707 <https://doi.org/10.3390/GEOSCIENCES10120488>, 2020.
- 708 Karakas, G., Kocaman, S., and Gokceoglu, C.: On the effect of dem quality for landslide  
709 susceptibility mapping, *ISPRS Annals of the Photogrammetry, Remote Sensing and Spatial*  
710 *Information Sciences*, V-3–2022, 525–531, [https://doi.org/10.5194/ISPRS-ANNALS-V-3-2022-](https://doi.org/10.5194/ISPRS-ANNALS-V-3-2022-525-2022)  
711 *525-2022*, 2022.
- 712 Kraemer, H. C.: Kappa Coefficient, *Wiley StatsRef: Statistics Reference Online*, 1–4,  
713 <https://doi.org/10.1002/9781118445112.STAT00365.PUB2>, 2015.
- 714 Liu, K., Song, C., Ke, L., Jiang, L., Pan, Y., and Ma, R.: Global open-access DEM performances  
715 in Earth’s most rugged region High Mountain Asia: A multi-level assessment, *Geomorphology*,  
716 338, 16–26, <https://doi.org/10.1016/J.GEOMORPH.2019.04.012>, 2019.
- 717 Loche, M., Alvioli, M., Marchesini, I., and Lombardo, L.: Landslide Susceptibility within the  
718 binomial Generalized Additive Model, in: *European Geosciences Union (EGU23)*,  
719 <https://doi.org/10.13140/RG.2.2.14089.62565>, 2023.
- 720 Lombardo, L. and Tanyas, H.: Chrono-validation of near-real-time landslide susceptibility  
721 models via plug-in statistical simulations, *Eng Geol*, 278,  
722 <https://doi.org/10.1016/J.ENGCEO.2020.105818>, 2020.
- 723 Lombardo, L., Bakka, H., Tanyas, H., van Westen, C., Mai, P. M., and Huser, R.: Geostatistical  
724 Modeling to Capture Seismic-Shaking Patterns From Earthquake-Induced Landslides, *J*  
725 *Geophys Res Earth Surf*, 124, 1958–1980, <https://doi.org/10.1029/2019JF005056>, 2019.
- 726 Lombardo, L., Opitz, T., Ardizzone, F., Guzzetti, F., and Huser, R.: Space-time landslide  
727 predictive modelling, <https://doi.org/10.1016/j.earscirev.2020.103318>, October 2020.
- 728 Mahalingam, R. and Olsen, M. J.: Evaluation of the influence of source and spatial resolution of  
729 DEMs on derivative products used in landslide mapping, *Geomatics, Natural Hazards and Risk*,  
730 7, 1835–1855, <https://doi.org/10.1080/19475705.2015.1115431>, 2016.
- 731 Meadows, M., Jones, S., and Reinke, K.: Vertical accuracy assessment of freely available global  
732 DEMs (FABDEM, Copernicus DEM, NASADEM, AW3D30 and SRTM) in flood-prone  
733 environments, *Int J Digit Earth*, 17, <https://doi.org/10.1080/17538947.2024.2308734>, 2024.
- 734 Muralikrishnan, S., Pillai, A., Narender, B., Reddy, S., Venkataraman, V. R., and Dadhwal, V. K.:  
735 Validation of Indian National DEM from Cartosat-1 Data, *Journal of the Indian Society of*  
736 *Remote Sensing*, 41, 1–13, <https://doi.org/10.1007/S12524-012-0212-9/FIGURES/13>, 2013.



- 737 Osama, N., Shao, Z., and Freeshah, M.: The FABDEM Outperforms the Global DEMs in  
738 Representing Bare Terrain Heights, *Photogramm Eng Remote Sensing*, 89, 613–624,  
739 <https://doi.org/10.14358/PERS.23-00026R2>, 2023.
- 740 Pawluszek, K. and Borkowski, A.: Impact of DEM-derived factors and analytical hierarchy  
741 process on landslide susceptibility mapping in the region of Rożnów Lake, Poland, *Natural*  
742 *Hazards*, 86, 919–952, <https://doi.org/10.1007/S11069-016-2725-Y/FIGURES/26>, 2017.
- 743 Pirasteh, S. and Li, J.: Landslides investigations from geoinformatics perspective: quality,  
744 challenges, and recommendations, *Geomatics, Natural Hazards and Risk*, 8, 448–465,  
745 <https://doi.org/10.1080/19475705.2016.1238850>, 2017.
- 746 Polidori, L. and Hage, M. El: Digital Elevation Model Quality Assessment Methods: A Critical  
747 Review, *Remote Sens (Basel)*, 12, <https://doi.org/10.3390/RS12213522>, 2020.
- 748 Pulighe, G. and Fava, F.: DEM extraction from archive aerial photos: accuracy assessment in  
749 areas of complex topography, *Eur J Remote Sens*, 46, 363–378,  
750 <https://doi.org/10.5721/EuJRS20134621>, 2013.
- 751 Purinton, B. and Bookhagen, B.: Validation of digital elevation models (DEMs) and comparison  
752 of geomorphic metrics on the southern Central Andean Plateau, *Earth Surface Dynamics*, 5,  
753 211–237, <https://doi.org/10.5194/ESURF-5-211-2017>, 2017.
- 754 Qin, C. Z., Bao, L. L., Zhu, A. X., Wang, R. X., and Hu, X. M.: Uncertainty due to DEM error in  
755 landslide susceptibility mapping, *International Journal of Geographical Information Science*, 27,  
756 1364–1380, <https://doi.org/10.1080/13658816.2013.770515>, 2013.
- 757 Qiu, H., Zhu, Y., Zhou, W., Sun, H., He, J., and Liu, Z.: Influence of DEM resolution on  
758 landslide simulation performance based on the Scoops3D model, *Geomatics, Natural Hazards*  
759 *and Risk*, 13, 1663–1681, <https://doi.org/10.1080/19475705.2022.2097451>, 2022.
- 760 Reichenbach, P., Rossi, M., Malamud, B. D., Mihir, M., and Guzzetti, F.: A review of  
761 statistically-based landslide susceptibility models, *Earth Sci Rev*, 180, 60–91,  
762 <https://doi.org/10.1016/J.EARSCIREV.2018.03.001>, 2018.
- 763 Riley, S. J., Degloria, S. D., and Elliot, S. D.: A Terrain Ruggedness Index that Quantifies  
764 Topographic Heterogeneity, *Intermountain Journal of Sciences*, 5, 23–27, 1999.
- 765 Saleem, N., Enamul Huq, M., Twumasi, N. Y. D., Javed, A., and Sajjad, A.: Parameters Derived  
766 from and/or Used with Digital Elevation Models (DEMs) for Landslide Susceptibility Mapping  
767 and Landslide Risk Assessment: A Review, *ISPRS Int J Geoinf*, 8, 545,  
768 <https://doi.org/10.3390/IJGI8120545>, 2019.
- 769 Schlögel, R., Marchesini, I., Alvioli, M., Reichenbach, P., Rossi, M., and Malet, J. P.: Optimizing  
770 landslide susceptibility zonation: Effects of DEM spatial resolution and slope unit delineation on  
771 logistic regression models, *Geomorphology*, 301, 10–20,  
772 <https://doi.org/10.1016/J.GEOMORPH.2017.10.018>, 2018.
- 773 Singhal, A.: Modern Information Retrieval: A Brief Overview, *IEEE Data Eng. Bull.*, 24, 35–43,  
774 2001.
- 775 Steger, S., Moreno, M., Crespi, A., Zellner, P. J., Gariano, S. L., Brunetti, M. T., Melillo, M.,  
776 Peruccacci, S., Marra, F., Kohrs, R., Goetz, J., Mair, V., and Pittore, M.: Deciphering seasonal  
777 effects of triggering and preparatory precipitation for improved shallow landslide prediction  
778 using generalized additive mixed models, *Natural Hazards and Earth System Sciences*, 23,  
779 1483–1506, <https://doi.org/10.5194/NHESS-23-1483-2023>, 2023.



- 780 Strobl, P. A., Bielski, C., Guth, P. L., Grohmann, C. H., Muller, J. P., López-Vázquez, C., Gesch,  
781 D. B., Amatulli, G., Riazanoff, S., and Carabajal, C.: The digital elevation model  
782 intercomparison experiment demix, a community-based approach at global dem benchmarking,  
783 International Archives of the Photogrammetry, Remote Sensing and Spatial Information  
784 Sciences - ISPRS Archives, 395–400, [https://doi.org/10.5194/ISPRS-ARCHIVES-XLIII-B4-](https://doi.org/10.5194/ISPRS-ARCHIVES-XLIII-B4-2021-395-2021)  
785 [2021-395-2021](https://doi.org/10.5194/ISPRS-ARCHIVES-XLIII-B4-2021-395-2021), 2021.
- 786 Takaku, J., Tadono, T., and Tsutsui, K.: Generation of high resolution global DSM from ALOS  
787 PRISM, International Archives of the Photogrammetry, Remote Sensing and Spatial Information  
788 Sciences - ISPRS Archives, 40, 243–248, <https://doi.org/10.5194/isprsarchives-XL-4-243-2014>,  
789 2014.
- 790 Tarquini, S., Isola, I., Favalli, M., Mazzarini, F., Bisson, M., Pareschi, M. T., and Boschi, E.:  
791 TINITALY/01: a new Triangular Irregular Network of Italy, *Annals of Geophysics*, 50, 407–425,  
792 <https://doi.org/10.4401/ag-4424>, 2007.
- 793 Tarquini, S., Isola, I., Favalli, M., Battistini, A., and Dotta, G.: TINITALY, a digital elevation  
794 model of Italy with a 10 meters cell size (Version 1.1) [Data set],  
795 <https://doi.org/https://doi.org/10.13127/tinality/1.1>, 2023.
- 796 Titti, G., Borgatti, L., Zou, Q., Cui, P., and Pasuto, A.: Landslide susceptibility in the Belt and  
797 Road Countries: continental step of a multi-scale approach, *Environ Earth Sci*, 80, 1–18,  
798 <https://doi.org/10.1007/S12665-021-09910-1/FIGURES/11>, 2021a.
- 799 Titti, G., van Westen, C., Borgatti, L., Pasuto, A., and Lombardo, L.: When Enough Is Really  
800 Enough? On the Minimum Number of Landslides to Build Reliable Susceptibility Models,  
801 *Geosciences (Basel)*, 11, 469, <https://doi.org/10.3390/GEOSCIENCES11110469>, 2021b.
- 802 Titti, G., Sarretta, A., Lombardo, L., Crema, S., Pasuto, A., and Borgatti, L.: Mapping  
803 Susceptibility With Open-Source Tools: A New Plugin for QGIS, *Front Earth Sci (Lausanne)*,  
804 10, 842425, <https://doi.org/10.3389/FEART.2022.842425/BIBTEX>, 2022.
- 805 Trevisani, S. and Cavalli, M.: Topography-based flow-directional roughness: Potential and  
806 challenges, *Earth Surface Dynamics*, 4, 343–358, <https://doi.org/10.5194/ESURF-4-343-2016>,  
807 2016.
- 808 Trevisani, S. and Rocca, M.: MAD: robust image texture analysis for applications in high  
809 resolution geomorphometry, *Comput Geosci*, 81, 78–92,  
810 <https://doi.org/10.1016/J.CAGEO.2015.04.003>, 2015.
- 811 Trevisani, S., Teza, G., and Guth, P.: A simplified geostatistical approach for characterizing key  
812 aspects of short-range roughness, *Catena (Amst)*, 223, 106927,  
813 <https://doi.org/10.1016/J.CATENA.2023.106927>, 2023a.
- 814 Trevisani, S., Skrypitsyna, T. N., and Florinsky, I. V.: Global digital elevation models for terrain  
815 morphology analysis in mountain environments: insights on Copernicus GLO-30 and ALOS  
816 AW3D30 for a large Alpine area, *Environ Earth Sci*, 82, [https://doi.org/10.1007/s12665-023-](https://doi.org/10.1007/s12665-023-10882-7)  
817 [10882-7](https://doi.org/10.1007/s12665-023-10882-7), 2023b.
- 818 Trevisani, S., Teza, G., and Guth, P. L.: Hacking the topographic ruggedness index,  
819 *Geomorphology*, 439, 108838, <https://doi.org/10.1016/J.GEOMORPH.2023.108838>, 2023c.
- 820 Trigila, A., Iadanza, C., and Spizzichino, D.: Quality assessment of the Italian Landslide  
821 Inventory using GIS processing, *Landslides*, 7, 455–470, [https://doi.org/10.1007/S10346-010-](https://doi.org/10.1007/S10346-010-0213-0/FIGURES/12)  
822 [0213-0/FIGURES/12](https://doi.org/10.1007/S10346-010-0213-0/FIGURES/12), 2010.



- 823 Van Westen, C. J., Rengers, N., Terlien, M. T. J., and Soeters, R.: Prediction of the occurrence of  
824 slope instability phenomena through GIS-based hazard zonation, *Geologische Rundschau*, 86,  
825 404–414, <https://doi.org/10.1007/S005310050149/METRICS>, 1997.
- 826 Wilson, J. P. and Gallant, J. C. (Eds.): *Terrain analysis : principles and applications*, John Wiley  
827 & Sons, Inc, 2000.
- 828 Zhang, K., Gann, D., Ross, M., Robertson, Q., Sarmiento, J., Santana, S., Rhome, J., and Fritz,  
829 C.: Accuracy assessment of ASTER, SRTM, ALOS, and TDX DEMs for Hispaniola and  
830 implications for mapping vulnerability to coastal flooding, *Remote Sens Environ*, 225, 290–306,  
831 <https://doi.org/10.1016/J.RSE.2019.02.028>, 2019.
- 832 Zingaro, M., La Salandra, M., Colacicco, R., Roseto, R., Petio, P., and Capolongo, D.:  
833 Suitability assessment of global, continental and national digital elevation models for  
834 geomorphological analyses in Italy, *Transactions in GIS*, 25, 2283–2308,  
835 <https://doi.org/10.1111/TGIS.12845>, 2021.
- 836
- 837